

Observed Boundary Layer Wind Structure and Balance in the Hurricane Core. Part I: Hurricane Georges

JEFFREY D. KEPERT

Bureau of Meteorology Research Centre, Melbourne, Australia

(Manuscript received 27 April 2005, in final form 12 December 2005)

ABSTRACT

The GPS dropsonde allows observations at unprecedentedly high horizontal and vertical resolution, and of very high accuracy, within the tropical cyclone boundary layer. These data are used to document the boundary layer wind field of the core of Hurricane Georges (1998) when it was close to its maximum intensity. The spatial variability of the boundary layer wind structure is found to agree very well with the theoretical predictions in the works of Kepert and Wang. In particular, the ratio of the near-surface wind speed to that above the boundary layer is found to increase inward toward the radius of maximum winds and to be larger to the left of the track than to the right, while the low-level wind maximum is both more marked and at lower altitude on the left of the storm track than on the right. However, the expected supergradient flow in the upper boundary layer is not found, with the winds being diagnosed as close to gradient balance.

The tropical cyclone boundary layer model of Kepert and Wang is used to simulate the boundary layer flow in Hurricane Georges. The simulated wind profiles are in good agreement with the observations, and the asymmetries are well captured. In addition, it is found that the modeled flow in the upper boundary layer at the eyewall is barely supergradient, in contrast to previously studied cases. It is argued that this lack of supergradient flow is a consequence of the particular radial structure in Georges, which had a comparatively slow decrease of wind speed with radius outside the eyewall. This radial profile leads to a relatively weak gradient of inertial stability near the eyewall and a strong gradient at larger radii, and hence the tropical cyclone boundary layer dynamics described by Kepert and Wang can produce only marginally supergradient flow near the radius of maximum winds. The lack of supergradient flow, diagnosed from the observational analysis, is thus attributed to the large-scale structure of this particular storm. A companion paper presents a similar analysis for Hurricane Mitch (1998), with contrasting results.

1. Introduction

The boundary layer (BL) is crucial for understanding tropical cyclone (TC) impact, since it is the “habitation layer” (Jelesnianski 1993) in which we and our infrastructure reside. In addition, turbulent processes within the BL transfer momentum to the ocean, generating damaging storm surge and waves, and also transfer energy from the oceanic reservoir to the TC heat engine, generating and maintaining the storm (Emanuel 1986). Yet, apart from the immediate surface, the structure of the tropical cyclone boundary layer (TCBL) has been less thoroughly characterized by observations than the rest of the storm. This lack of observational coverage is

partly due to safety, since aircraft are unable to fly too near the surface in an intense TC. In addition, Doppler radar is subject to sea clutter, cannot see right to the surface, and has insufficient resolution to resolve the large gradients there. Instruments on tall towers and wind profiling radars rely on the relatively compact TC core happening to pass over the site. Finally, the previous generation of aircraft-deployed dropsondes, which used the Omega radio navigation system, required heavy vertical filtering to remove noise, and so had insufficient vertical resolution to resolve the strong gradients near the surface (Hock and Franklin 1999).

The recent advent of the global positioning system (GPS) dropsonde (Hock and Franklin 1999) has provided a hitherto unprecedented observational coverage in the tropical cyclone boundary layer. This instrument uses GPS navigation and radiosonde-type pressure, temperature, and humidity sensors to provide soundings with the unprecedented vertical sampling rate of 2 Hz,

Corresponding author address: Dr. Jeff Kepert, Bureau of Meteorology Research Centre, GPO Box 1289K Melbourne, 700 Collins Street, Docklands, VIC 3001, Australia.
E-mail: j.kepert@bom.gov.au

or approximately 6 m. Up to four instruments may be in action simultaneously, which with the fast fall rate of about 12 m s^{-1} and relatively low unit cost allows a high density of measurement. These instruments have been routinely deployed from U.S. hurricane reconnaissance aircraft since 1997, with over 5000 having been used to date in the North Atlantic Ocean. They have proved to be highly reliable, with the only significant problem being a tendency for the wind measurements to fail in the lowest few tens of meters in the eyewall of intense hurricanes (Franklin et al. 2003; Powell et al. 2003), and a dry humidity bias in the early models, since corrected (Wang et al. 2002).

This wealth of new wind data has so far been the subject of two published analyses. Franklin et al. (2003) presented a statistical analysis of the surface wind factor (SWF; the ratio of the 10-m wind speed to that at some reference height in the free atmosphere) for dropsonde data from the 1997–99 Atlantic hurricane seasons. They showed that the SWF is larger beneath the eyewall than at larger radii, and is also larger when calculated relative to 850-hPa winds than for 700-hPa winds. While the latter is at least partly due to the cyclone's warm core, the reasons for the former are less obvious, although it is of considerable practical significance. For instance, their recommendation that the surface wind beneath the eyewall be estimated as 90% of the 700-hPa wind was a major part of the justification for the reanalysis of Hurricane Andrew's intensity at landfall from category 4 to 5 on the Saffir–Simpson scale (Landsea et al. 2004). Powell et al. (2003) concentrated on the air–sea interface, using the same data as Franklin et al. to calculate drag coefficients in TC conditions and found that the drag coefficient increased with wind speed up to about 40 m s^{-1} , consistent with existing parameterizations, but then decreased markedly at stronger winds. These two studies both analyzed a large body of data across many storms, without considering the particular characteristics of individual TCs, although there is known to be substantial variation from storm to storm. Thus, the first purpose of the present papers [see also Kepert (2006), hereafter Part II] is to present and compare detailed analyses of the wind field in the BL of two intense TCs.

Perhaps because of the lack of verifying observations, the BL has received less theoretical attention than other parts of the TC. The one-dimensional model of Powell (1980; updated in Powell et al. 1996) has been extensively used to estimate near-surface winds from flight-level observations. Two-dimensional axisymmetric models include the analytical model of Rosenthal (1962) and the numerical models of Anthes (1971),

Eliassen and Lystad (1977), and Montgomery et al. (2001). Important results of these studies include that the BL depth declines markedly toward the center of the storm. Shapiro (1983) presented a two-dimensional depth-averaged model that resolved the motion-induced asymmetry. More recently, Kepert (2001, henceforth K01) and Kepert and Wang (2001, henceforth KW01) presented three-dimensional analytical and numerical models of the TCBL, which resolve the vertical structure of the motion-induced asymmetry. The majority of these studies, including K01 and KW01, diagnose the boundary layer flow by solving the dry equations of motion subject to a prescribed, constant with height, pressure field representative of a tropical cyclone. Differences between the models are due to (i) whether axisymmetry is assumed, (ii) whether the equations are depth averaged, (iii) the parameterizations of turbulence and surface fluxes used, (iv) the intensity and structure of the gradient-level forcing flow, and (v) the method of solution. The numerical models typically find the solution by integrating the equations forward in time until a quasi-steady state is achieved, while the analytic models set the time derivative terms to 0 and make further simplifying assumptions to facilitate solution. Specifically, Rosenthal (1962) and K01 are respectively axisymmetric and three-dimensional linearized analytic models with simple turbulence and surface stress parameterizations, while Kuo (1971, 1982) is axisymmetric but uses a series expansion technique instead of a linearization. Of the numerical models, Anthes (1971) is axisymmetric, Shapiro (1983) is depth averaged with a truncated spectral representation of the asymmetries, and KW01 is fully three-dimensional and additionally has sophisticated parameterizations of the turbulent and surface exchange processes. Eliassen and Lystad (1977) and Montgomery et al. (2001) take a slightly different approach, calculating the BL flow of a vortex that is slowly spinning down due to surface friction. All these studies diagnose the BL flow as the response to a gradient-level forcing, while Shapiro (1983), K01, and KW01 consider also the forcing due to storm motion. The diagnosed BL structure is unable to influence the prescribed forcing; thus these models represent one side of what in reality is a two-way interaction. Further, as they neglect moisture, the effects of moist dynamics on the BL are not represented.

Kepert (2001) and Kepert and Wang (2001) used their models to make some potentially important predictions regarding TCBL winds:

- The SWF increases from 0.6 to 0.7 in the outer core to 0.8 to 1.0 near the eyewall, and is greater on the

left of the storm than on the right (in the Northern Hemisphere).

- The azimuthal-mean azimuthal wind in the upper BL is slightly supergradient in the cyclone periphery, and increasingly so near the core, depending on the storm intensity and structure.
- This low-level jet is more strongly supergradient on the left (right) side of a moving storm in the Northern (Southern) Hemisphere.
- The BL depth decreases from around 1.5 km at 2.5 times the radius of maximum winds (RMW) to about 500 m in the inner core.

Note that Zhang et al. (2001) also found azimuthal-mean supergradient flow at the top of the BL near the eyewall in their simulation of Hurricane Andrew's landfall. This theoretical progress has coincided with the advent of sufficient data to test it, and so further aims of the present papers are to test these predictions against the GPS dropsonde data in Hurricanes Georges and Mitch, to use the theory presented by K01 and KW01 to understand the differences in BL structure between these storms, and to examine the ability of KW01's model to simulate the BL flow in these storms.

Some of the above predictions, such as the predicted difference in shape of the BL wind vertical profile between the left and right sides of the storm, and the spatial SWF structure, should be easy to check. Indeed, the results of Franklin et al. (2003) support the radial variation of SWF, and found a left-right asymmetry of 4%, similar to but smaller than K01's and KW01's predictions. However, verifying that the winds in the upper BL are supergradient demands more thorough analysis. It is necessary to determine not only the extent to which the wind is supergradient, but also our confidence that any apparent imbalance is real, and not an artifact of the observations or analysis.

Previous observational analyses of gradient-wind balance in TCs include Gray (1967) and Gray and Shea (1973), who composited aircraft winds at two levels in several storms relative to the RMW and compared the vertical shear to the observed horizontal temperature gradient using the thermal wind equation in cylindrical coordinates. This approach was necessary because the winds were derived from Doppler radar measurement of the aircraft motion relative to the sea surface, which introduced a systematic but unknown bias due to the surface drift, removed by subtracting winds at two levels. They found the winds were supergradient at all levels immediately inside of the RMW, with a larger imbalance at 900 hPa than aloft.

Willoughby (1990) used more accurate winds from inertial navigation equipment, composited data from

individual storms over a period of typically 6 h, and relative to distance from the center of the storm. He presented analyses for 13 storms, and found no evidence of supergradient flow.

Gray's (1991) comment on Willoughby's (1990) results largely re-presented his earlier work, while Willoughby's (1991) reply included some further storms and emphasized shortcomings in Gray's analysis technique, notably the compositing relative to the RMW and across several storms. On the other hand, Gray pointed out that the majority of Willoughby's flights were at 850 or 700 hPa, while his included a significant amount of 900-hPa data, and suggested that the lower level was more conducive to supergradient flow.

Mitsuta et al. (1988) analyzed observations from flat coral islands to the south of Japan in two typhoons, and showed that the 10-m wind could exceed the gradient wind just inside the RMW. They suggested that this effect was due to strong inflow and advection of angular momentum.

The purpose of this two-part paper is to present a detailed analysis of the wind field structure and balance within the BL of two intense hurricanes, Georges and Mitch of 1998, to compare these analyses with the predictions of K01 and KW01, and to provide explanations for the observed structures. This paper will describe the data and analysis techniques used, and present the results for Hurricane Georges, while the results for Mitch are in Part II, along with the concluding discussion. In this part, section 2 gives a brief overview of Hurricane Georges, introduces the data used in this analysis, and describes the processing techniques. The wind field structure is described in section 3 and gradient balance is analyzed in section 4. Direct comparison to the model of KW01 is made in section 5, and conclusions are drawn in section 6.

2. Storm synopsis and data coverage

Hurricane Georges of 1998 was a major hurricane that reached a peak intensity of 135 kt shortly after the period analyzed here. This section briefly describes the life cycle of Georges, and the two aircraft reconnaissance missions that took the measurements analyzed here. For further details, refer to Pasch et al. (2001), Aberson (1998), and Black (1998).

Hurricane Georges (see Fig. 1 for the track) formed from an easterly wave that crossed the coast of Senegal on 13 September 1998. The system reached tropical depression status on the 15th, and intensified further as it moved toward the west-northwest (WNW), reaching hurricane intensity on the 18th. Intensification became more rapid on the 19th under the influence of an upper-

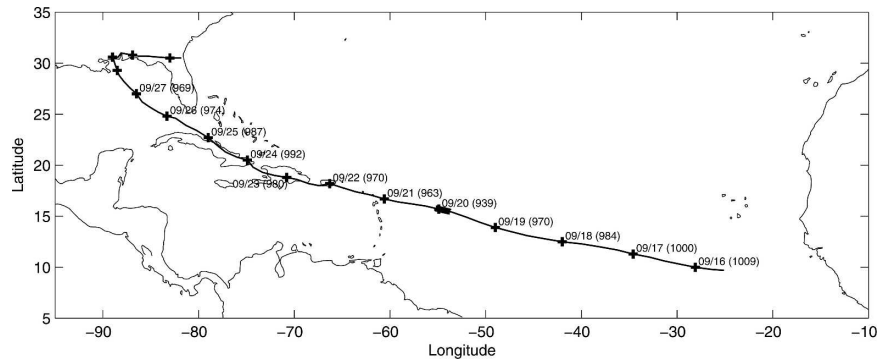


FIG. 1. The best-track analysis for Hurricane Georges from the U.S. National Hurricane Center. Tick marks show the month, day, and estimated central pressure (hPa) at 0000 UTC, while the heavy section of the track near 20 September shows the duration of the missions being analyzed here.

level anticyclone, associated with very weak vertical shear, which tended northwesterly then gradually strengthened to 7 m s^{-1} for the 850–200-hPa shear by 0000 UTC on the 20th.¹ The storm reached its peak intensity of 135 kt, with a central pressure of 937 hPa, at 0600 UTC on the 20th. That this moderate value of wind shear did not immediately cause the storm to weaken is consistent with Frank and Ritchie (2001), who found for similar values of shear a time lag of about a day between the shear onset and storm weakening, and with Reasor et al. (2004), who predicted that intense cyclones can resist modest shear, depending on their vorticity gradient. Georges subsequently weakened markedly as the shear strengthened, before making its first (of seven) landfall on Antigua at 0430 UTC on the 21st.

A three-aircraft mission was flown into Georges by the National Oceanographic and Atmospheric Administration (NOAA) from late on the 19th, into the early 20th. The goals of the mission were to measure the synoptic flow surrounding Georges, and for two aircraft to deploy GPS dropsondes in the cyclone core. The first (Black 1998) began its initial “figure-4 pattern” through the core at approximately 4.5-km altitude at 1911 UTC on the 19th, beginning about 90 km to the west of the eye. A west–east pass through the eye was followed by north–south and south–north passes, each extending about 80 km from the center and finishing at 2037 UTC. Eight dropsondes were deployed in the eyewall and

four at the ends of the radial flight legs, with good performance although the eyewall wind measurements tended to fail in the lowest few tens of meters. The second set of core measurements began at about 0000 UTC on the 20th (Aberson 1998) to the southeast of the eye, at a similar altitude. A single figure-4 pattern was flown during which 16 dropsondes were deployed, with similar performance. The aircraft tracks and dropsonde release points are shown in Fig. 2; further dropsonde details may be found in Kepert (2002, his Table 4.1). The two core observation periods will be referred to as the early and late periods. A reconnaissance flight conducted by the U.S. Air Force at approximately 700 hPa, partially overlapped the early period, and deployed another three dropsondes in the eye and eyewall, which were also included.

The data used in this analysis were the following:

- Thirty-one GPS dropsonde soundings, obtained in postprocessed, quality-controlled form from the Hurricane Research Division (HRD) of NOAA. These soundings consist of measurements of temperature, humidity, pressure, wind, and location at 0.5-s intervals, or approximately 6 m vertically. The aircraft radar and pressure altitudes at release and an estimate of the height of the last pressure observation (usually less than 10 m) are also provided, either of which can provide a boundary condition for a hydrostatic integration. The latter can also be used to estimate a surface pressure, here called the splash pressure. Full details of the dropsonde system are given by Hock and Franklin (1999).
- Aircraft measurements of three-dimensional wind, thermodynamic, and storm track data, and several radar composite images from the lower-fuselage radar. The winds were storm-relative in cylindrical co-

¹ Environmental wind hodographs were averaged over a 200–800-km annulus centered on the storm, using data from the ERA-40 reanalysis. This averaging domain was recommended by DeMaria and Kaplan (1999) and is currently used for calculating environmental shear in the Statistical Hurricane Intensity Prediction System (J. Kaplan 2004, personal communication).

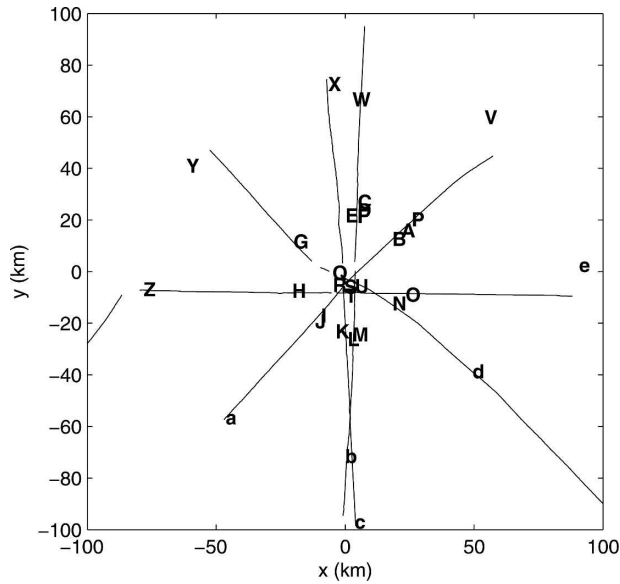


FIG. 2. The aircraft reconnaissance “radial legs” and deployment points of dropsondes used in this study, in storm-relative coordinates.

ordinates, relative to a track found as in Willoughby and Chelmow (1982), averaged into 0.5-km radius bins for each of the 10 radial legs flown. They were converted back into earth-relative coordinates for this study. Airborne Doppler radar velocity measure-

ments were not used because volume averaging and sea clutter limit the utility of these data in the high gradients near the sea surface. The aircraft data systems are described by Jorgensen (1984).

- Analyses of wind and geopotential from the European Centre for Medium-Range Weather Forecasts (ECMWF) 40-yr Re-Analysis project (ERA-40; Simmons and Gibson 2000), interpolated to a 2.5° grid on standard pressure levels, at 12-h intervals.

Times were expressed relative to 2100 UTC on 19 September 1998, and data were renavigated into a Cartesian coordinate system with origin at 15.55°N, 54.20°W, the location of Georges at this time according to the National Hurricane Center (NHC) best-track analysis.

During these observations, Hurricane Georges had a well-defined eye with a highly symmetric inner core, as shown by radar (Fig. 3). Visible, IR, and microwave satellite imagery (not shown) of Georges showed a large circular eye surrounded by a nearly uniform ring of deep convection with little evidence of spiral bands outside this ring. Georges was subject to weak southeasterly environmental shear during at least the first part of this period, which opposes the beta-gyre-induced shear and contributes to the symmetry of the storm (Knaff et al. 2003). Georges was thus largely free of sources of asymmetry other than asymmetric fric-

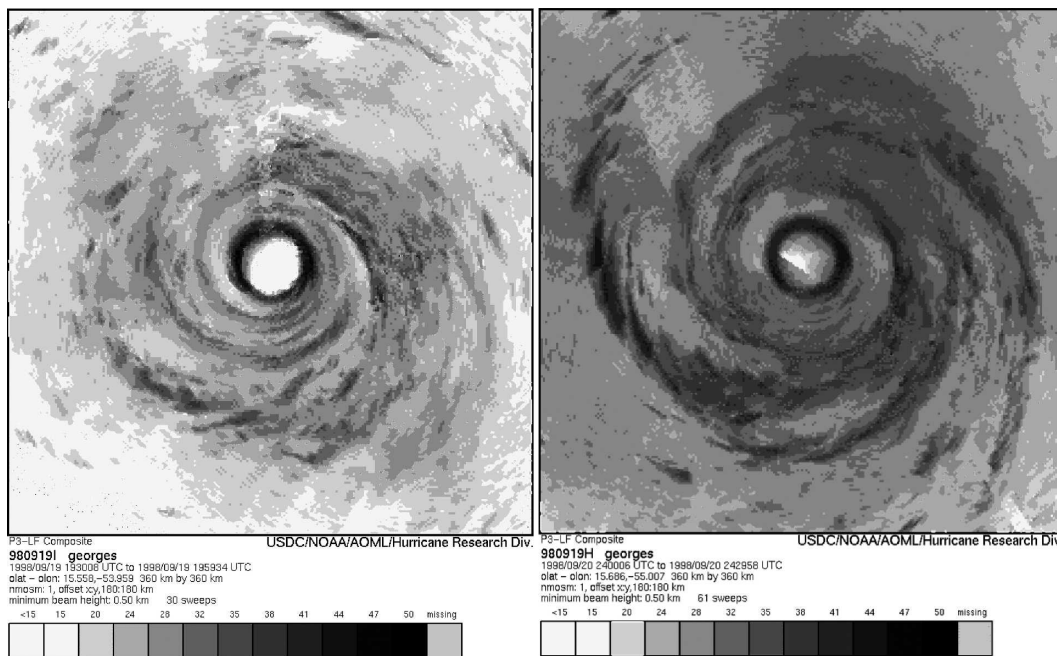


FIG. 3. Composite radar reflectivity image from NOAA reconnaissance aircraft (left) between 1930 and 1959 UTC on 19 Sep 1998 and (right) between 0006 and 0030 UTC 20 Sep 1998. Image size is 360 km square. Courtesy of NOAA HRD.

tion, and is therefore a good candidate for testing the theory of K01 and KW01. In the absence of other causes, the low-level wind asymmetry should be well-explained by the motion, while the relative symmetry of the storm and good data coverage makes Georges a good candidate for an analysis of the azimuthally averaged gradient balance.

a. Cyclone track

Analyzing gradient balance near the eyewall of a TC places significant demands on the analysis accuracy, particularly in locating the observations relative to the cyclone. For instance, if the RMW is 40 km, an error in the cyclone track (or observation location) of 5 km will lead to a 12% error in the centripetal term in the gradient-wind equation, and thus to a 6% error in the derived gradient wind speed, which is an unacceptably large fraction of the extent to which the modeled winds were supergradient in KW01. Yet best-track databases typically give the cyclone position to 0.1 degree of latitude and longitude, or roughly 10 km, so round-off error alone can invalidate the analysis of gradient-wind balance. The problem of objectively finding the cyclone track from asynoptic data was considered by Kepert (2005), who extended the wind-based techniques of Willoughby and Chelmon (1982) and Marks et al. (1992) to allow the use of asynoptic data, and presented a new technique, the translating pressure fit (TPF), to locate the center and motion of the storm from asynoptic pressure data. These techniques each fit a linear track to the data, which Kepert (2005) notes is convenient as it does not add extra terms to the equations of motion, but may be inappropriate if the cyclone is experiencing a marked trochoidal oscillation. Kepert (2005) also showed that the use of pressure data was strongly preferable to wind data near the earth's surface because of the frictional inflow and wind asymmetry there, but produced similar results above the BL.

The storm tracks found by these methods, applied to flight-level wind and pressure observations and to surface pressure observations, are summarized in Table 1. The tracks fall into two groups, with the TPF tracks and those using storm-relative winds being nearly coincident and about 8 km to the north of and nearly parallel to those using earth-relative winds. This right-of-track displacement is expected on kinematic grounds, and the otherwise good agreement between methods improves confidence in their accuracy here. These tracks were also compared with the nonlinear track determined by the original Willoughby and Chelmon (1982, henceforth WC82) method, obtained with the aircraft data, which had a trochoidal oscillation of a few kilometers amplitude, a scale much smaller than the eye. The

TABLE 1. Storm tracks found by various methods for Hurricane Georges. Algorithm WC82 refers to the nonlinear track from the original Willoughby and Chelmon (1982) method, TWCW to the modified Willoughby and Chelmon (1982) method with asynoptic data and an improved observation-error specification, TMHG to the modified version of the simplex method of Marks et al. (1992) to use asynoptic data, and TPF to the translating-pressure-fit method, all as described in Kepert (2005). Here, SR refers to storm-relative and ER to earth-relative winds, FL to aircraft flight-level data from 1900 UTC 19 Sep to 0050 UTC 20 Sep, and SFC to dropsonde surface data from 1906 UTC 19 Sep to 0121 UTC 20 Sep. Tracks are in a Cartesian coordinate system centered on the NHC best-track position at 2100 UTC 19 Sep 1998. The final column gives the range in RMW over all flight-level radial legs, according to each track.

Technique	x_t (km)	y_t (km)	u_t (m s ⁻¹)	v_t (m s ⁻¹)	RMW range (km)
WC82	—	—	—	—	20.5–30.9
TWCW SR FL	-1.9	8.5	-7.03	1.45	22.3–30.4
TWCW ER FL	-2.3	4.4	-7.02	1.48	19.5–32.4
TMHG SR FL	-1.8	8.7	-7.06	1.39	22.3–30.4
TMHG ER FL	-2.2	2.5	-7.07	1.49	17.8–34.3
TPF FL	0.2	9.7	-7.05	1.31	24.0–28.7
TPF SFC	-1.8	9.0	-7.04	1.35	—

range of radii, over all flight legs, at which the maximum wind occurs, are also included in Table 1 and is least for the TPF track (even though this does not use wind data), strongly suggesting that it best depicts the motion of the storm on the scale of the RMW. Noting that WC82 and Bluestein and Marks (1987) state that it is relatively common for the WC82 center to be displaced from the geometric center of the radar eye, and that the WC82 method uses only data within about 5 km of the center, it seems that the trochoidal oscillation in the WC82 track is due to small-scale asymmetry within the eye, and is not representative of the storm motion as a whole. Kepert (2005) further discusses the impact of analysis scale on the diagnosed motion.

Figure 4 illustrates the importance of using an accurately determined track. Figure 4a shows the dropsonde surface pressure observations plotted against radius relative to the NHC best track, and has a large amount of scatter near the RMW. When plotted against radius relative to the TPF track (Fig. 4b), the observations lie much closer to a single curve. Thus estimates of the pressure gradient will be more accurate using the TPF track than the NHC best track.

A vortex tilt between flight level and the surface is apparent from the TPF tracks, and varies slightly from (-2.0, -0.9) km at the beginning of the observing period to (-1.9, -0.2) km at the end, with the surface center to the west-southwest (WSW) of the flight-level center. Care was taken to use the actual time of observation here, not of dropsonde release, since the TC

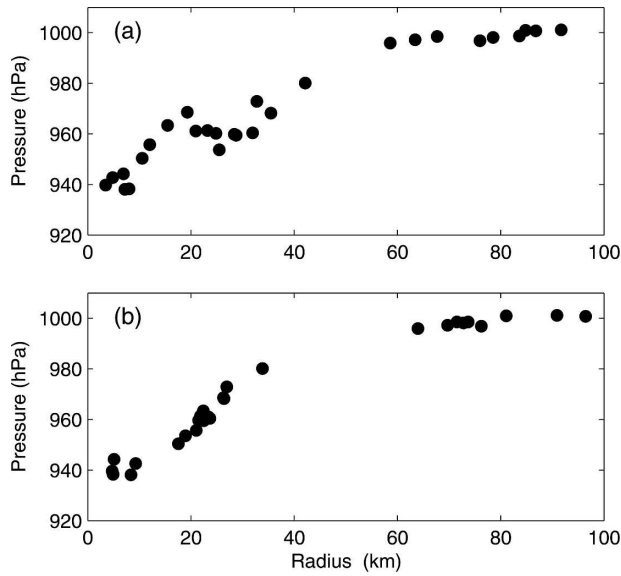


FIG. 4. Dropsonde splash surface pressures in the core of Hurricane Georges, as a function of radius. (a) Radius relative to the NHC best track. (b) Radius relative to the track determined from the pressure observations by the translating-pressure-fit method.

moved some 3 km during the typical fall duration of around 400 s. This tilt appears to be real because the surface pressure gradient at the RMW of Georges is about 2 hPa km^{-1} , so ignoring this 2-km displacement leads to an apparent 4-hPa azimuthal wavenumber-1 asymmetry in the surface pressure field, readily apparent if the surface pressure observations are located relative to the flight-level TPF track. The dropsonde and aircraft temperature data show a small eastward displacement of the otherwise symmetric warm core, hydrostatically consistent with this tilt.

For the descriptive part of this analysis, the TPF track obtained from the flight-level data will be used. Greater precision is needed for the analysis of gradient-wind balance and for that, this vortex tilt will be applied.

b. Hydrostatic integration of the dropsonde data

The dropsondes measure pressure, temperature, humidity, and motion. The geopotential height is calculated by integrating the hydrostatic equation, either upward from the surface or downward from the aircraft. For the upward integration the height of the last observation provides the integration constant, while the downward integration uses the aircraft's observed pressure and height, and also provides a second estimate of the surface pressure. Two important assumptions underlie these calculations: that the atmosphere is in hydrostatic balance, and that the dropsonde path is vertical. The second of these assumptions is not true and

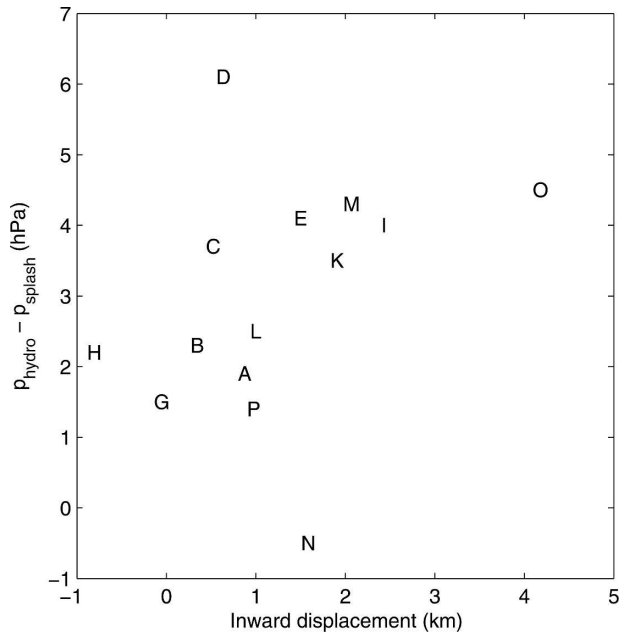


FIG. 5. Scatterplot of difference between hydrostatic surface pressure calculated by downward integration along the dropsonde trajectory and splash pressure, against inward displacement of the dropsonde trajectory, for near-eyewall sondes in Hurricane Georges.

must be corrected for. The eyewall dropsondes in Hurricane Georges typically rotated about 60° in azimuth as they fell, and had an inward displacement of up to 3 km, the bulk of which typically occurred in the lowest 500 m of the dropsonde trajectory. This radial displacement will introduce a systematic difference between upward and downward hydrostatic integrations, due to the surface pressure gradient of approximately 2 hPa km^{-1} at the RMW. This difference caused problems in analyzing the pressure gradient if a mix of upward and downward profiles is used, as the "upward" profiles had systematically lower pressures at any given height than the "downward" profiles, because their hydrostatic boundary condition points are closer to the storm center. In contrast, the azimuthal displacement can be neglected in this strongly axisymmetric system.

The effect of radial displacement can be seen in the relationship between the difference between the splash pressure and the surface pressure calculated by integrating the hydrostatic equation downward from the aircraft along the dropsonde trajectory. Figure 5 shows a near-linear relationship, although sondes D and N are outliers from this trend; the former was at a larger radius than either its release or splash radius for most of its fall, and so may have experienced unrepresentatively cold temperatures, biasing its hydrostatic surface pressure high, while the latter possibly because the rela-

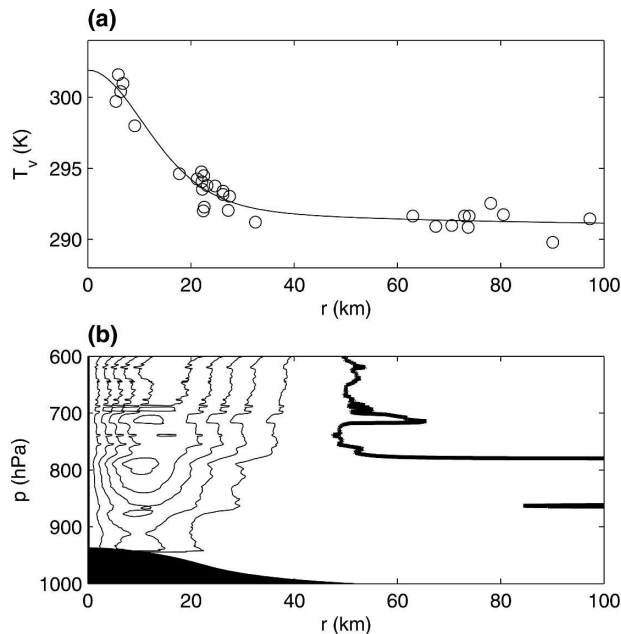


FIG. 6. (a) Dropsonde observations of T_v at 800 hPa as a function of radius in Hurricane Georges, together with fitted rational function as described in the text. (b) Radial virtual temperature gradient from the fitted curves. Contour interval 0.1 K km^{-1} , zero contour heavy.

tive humidity measurements were too high (comment by the mission scientist contained in the data file). There is also an offset of 1–2 hPa at zero radial displacement, which can be significantly reduced by correcting the aircraft altitude to a geopotential, since the gravitational acceleration at 15°N of $g = 9.7838 \text{ m s}^{-2}$, compared to the standard 9.80665 m s^{-2} , is equivalent to a difference of about 10 m in the release height.

To correct for the radial displacement and perform the hydrostatic integration at constant radius, it is necessary to account for the radial temperature gradient. The cyclone is warm cored, so the temperatures immediately above the splash point will normally be higher than those encountered by the falling sonde. To correct for this effect, the radial virtual temperature gradient estimated by fitting curves of the form

$$T_v(r) = \frac{a_0 + a_1 r^2 + a_2 r^4 + a_3 r^6}{(1 + br^2)^3} \quad (1)$$

to the temperature data. An example fit, together with the estimated radial temperature gradients for the whole domain, is shown in Fig. 6, where it can be seen that the curve adequately describes the radial temperature variation.

The estimated radial virtual temperature gradients were used to linearly adjust the dropsonde observations

TABLE 2. Mean and standard deviation of difference between the surface pressure estimated by a downward hydrostatic integration from flight level and the dropsonde splash pressure. The downward integration is done either along the dropsonde slant trajectory, or vertically, as described in the text. The latter approach produces a markedly reduced bias, and also a small improvement in scatter.

	Early period (hPa)	Late period (hPa)
Slant integration	2.46 ± 0.95	1.84 ± 0.91
Vertical integration	0.88 ± 0.82	0.25 ± 0.87

to the radius of the hydrostatic boundary condition point. The hydrostatic equation was then integrated to give the pressure–height relationship in that vertical column. The integration was carried out in both directions where possible, and it was found that the correlation between the radial displacement and the difference between the two surface pressure estimates (Fig. 5) was largely eliminated, as shown in Table 2. The upward integrations are used henceforth except where the dropsonde fails before impact. The derived pressure–height data for each sonde are applied at the location of the hydrostatic boundary condition point, not along the sonde trajectory.

3. The wind field

The dropsonde observations are divided into three groups, near the radius of maximum winds (radii 15–40 km), the inner eye (radius less than 15 km), and the outer core (radii 60–100 km). In this section, the measurements in each group are discussed, followed by analysis of the wind field and wind reduction factor.

a. The winds near the radius of maximum winds

The measured storm-relative azimuthal wind profiles from the 16 near-eyewall sondes are shown in Fig. 7 with their storm-relative positions (at 1-km height) and modeled profiles to be discussed in section 5. There is substantial variation between individual observed profiles, in both the broad shape of the profile and in the magnitude of the smaller-scale oscillations. However, it is clear that much of the large-scale variation between observed profiles relates to their position within the storm. The similarity between profiles that are close to each other (in a storm-relative sense) is more remarkable when one notes that these observations were taken over a period of over five hours. In particular, profiles N and O were taken almost 5 h apart, A and P over 4 h apart, and while I and J were separated by only 34 s, K was half an hour later. It is thus reasonable to con-

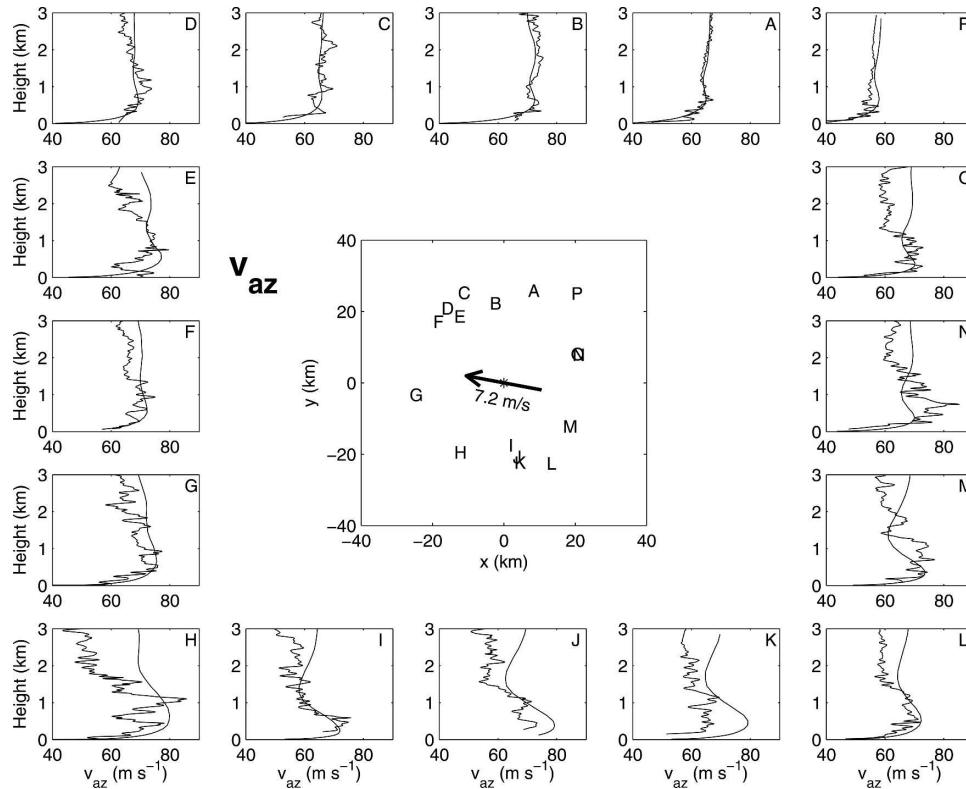


FIG. 7. Profiles of the storm-relative azimuthal wind component observed by dropsondes (curves with small-scale fluctuations) and represented in the model (smooth curves) in and near the eyewall of Hurricane Georges. The model values were interpolated from the model grid to the observed dropsonde trajectory. (center) The storm-relative position of each sonde as it fell through a height of 1 km and the storm motion are shown.

clude that the variability in measured wind profiles depends largely on location within the storm. The storm-relative azimuthal winds have a low-level maximum in all profiles, which is most marked to the south and east of the storm, where it is up to 20 m s^{-1} stronger than the winds in the upper part of the profile, and least marked to the north.

The storm-relative radial winds are shown in Fig. 8. Most of the profiles do not show zero radial flow at the top of the profile, which may be due to small errors in the track causing uncertainty in the decomposition into storm-relative winds, and to the deep thermally driven inflow above the BL. These factors complicate the interpretation of what, from the perspective of BL processes, is inflow and outflow. However, it seems that, starting from profile A and moving counterclockwise, that there is a tendency for the BL inflow to become deeper and stronger toward the front of the storm, together with the formation of an outflow layer above, which persists around the left and rear of the storm. This outflow layer is generally above the strongest azimuthal winds.

Much of the smaller-scale structure in the profiles is presumably turbulence. To remove these features, the profiles were averaged into 100-m layers, divided into four quadrants according to their position at a height of 1 km, and averaged. Averages over all 16 profiles were also calculated, and all are shown in Fig. 9. Averaged around the storm, the near-surface inflow layer is 1.1 km deep, with a secondary inflow layer above 2.2 km presumably forced by latent heat release in the eyewall (reviewed in Willoughby 1995). Marked outflow is present only to the southwest, although it seems reasonable to interpret the zero radial component just above 1 km in the eastern quadrants as being BL-forced outflow, relative to the thermally and shear-forced inflow aloft. This interpretation is consistent with K01 and KW01's results (they did not include these effects), and with the heights of the azimuthal flow maxima in the various quadrants.

The mean azimuthal wind over the whole annulus shows a broad maximum between about 500 and 1200 m. The flow decreases rapidly in the first few hundred meters above this layer, then more slowly. This change

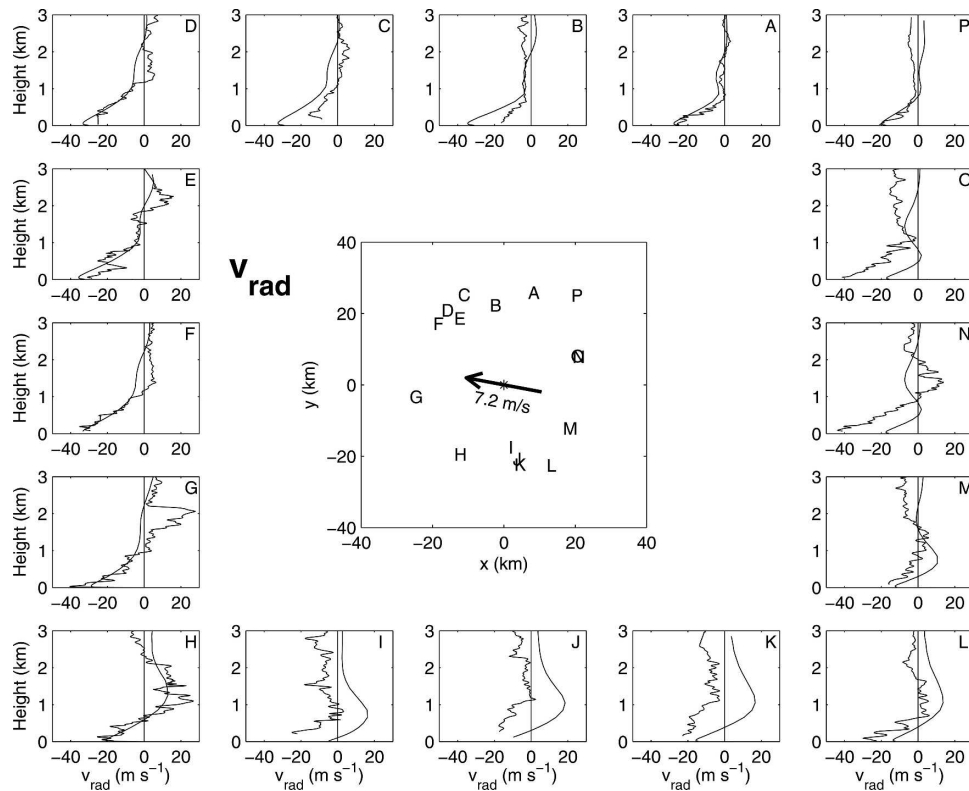


FIG. 8. Same as Fig. 7, except for the storm-relative radial wind component.

in shear could indicate that the maximum is supergradient, since gradient balance (and hydrostatic balance) implies thermal balance, and thus fairly constant shear above the BL unless the radial temperature gradient is greater immediately above the maximum than further aloft, which is implausible. However, since the size of the relatively sudden decrease immediately above the maximum is less than the standard deviation of the differences between profiles, it is difficult to be confident that the change in slope is real. Gradient-wind balance will be analyzed in detail below. The quadrant-mean azimuthal velocity profiles emphasize that the low-level jet is much more marked to the south of the storm (left of track) than to the north.

Mean profiles stratified by radius are shown in Fig. 10. The inner annulus (15–25-km radius) has a lower and more marked azimuthal maximum, stronger near-surface winds, and slightly shallower inflow, than the 25 to 40 km annulus, in good agreement with the theoretical predictions.

b. The winds in the eye

The profiles of storm-relative wind components for the five dropsondes in the eye are shown in Fig. 11. The

azimuthal wind is from 10 to 20 m s^{-1} at the surface, and either decreases or remains roughly constant with height. There is little evidence of a frictional retardation of the wind near the surface, consistent with theoretical work showing that the BL becomes very shallow in the eye of the cyclone (Rosenthal 1962; Eliassen and Lystad 1977; K01; KW01). The radial flow measurements show neither systematic variation nor consistency from profile to profile, possibly because the measurements are sampling small-scale, vertically coherent, but transient features.

c. The winds in the outer core

Averages of the storm-relative wind components for each quadrant, and overall, in the annulus between 40- and 100-km radius, are shown in Fig. 12. The overall mean shows an inflow layer a little over 1 km deep, with a suggestion of weak outflow centered near 1.5 km. The maximum mean azimuthal wind is below the top of the inflow layer at 800 m. This maximum is broader and stronger to the north of the storm than to the south, where it is comparatively weak, narrow, and closer to the surface. The inflow is deepest to the northeast, and the storm-relative outflow strongest, at about 5 m s^{-1} ,

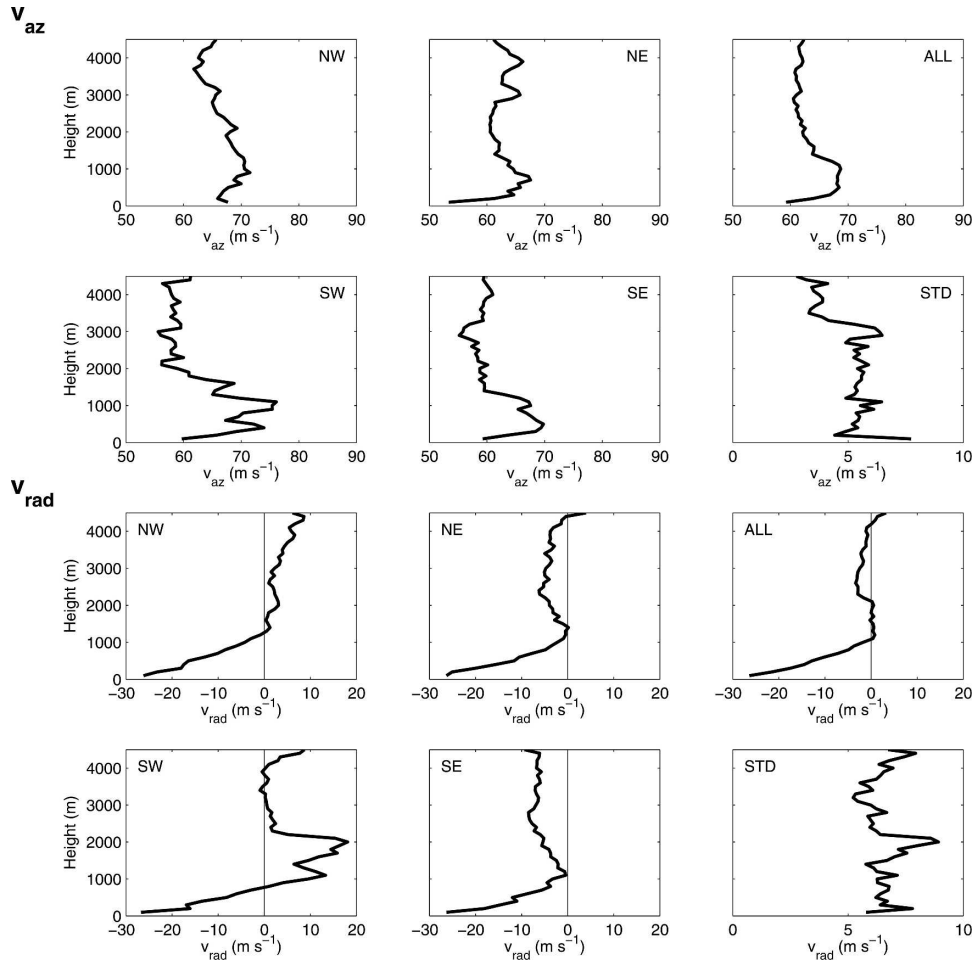


FIG. 9. Mean profiles of (top two rows) azimuthal and (bottom two rows) radial storm-relative wind, from dropsondes between 15- and 40-km radius. Each group of six panels contains averages over the four quadrants and the whole annulus as labeled. The panel labeled STD shows the standard deviation for the whole annulus.

in the two western quadrants, where it largely lies above the azimuthal wind maximum.

d. Horizontal wind analyses

Analyses of the storm-relative azimuthal and radial wind components were prepared using a multivariate statistical interpolation scheme (Lorenc 1981; Daley 1991, chapter 4). The background field for the azimuthal component was derived by applying the gradient wind equation to the symmetric pressure analyses from the next section, while the radial component had a symmetric inflow angle of 30° at the surface, decreasing linearly to 0° at 500 m. The analyses are only slightly sensitive to other reasonable choices of background. The background error correlation was modeled as in Daley (1985), applied to a second-order autoregressive function with length scale of 100 km. The background

error standard deviation was taken to be 5 m s⁻¹, equally partitioned between the rotational and divergent wind components. The wind profiles were smoothed by a low-pass filter with a cutoff wavelength of 50 m (vertical) to remove small-scale turbulence, and the observation errors were assumed to be independent with standard deviation of 3 m s⁻¹, a little larger than that given by Hock and Franklin (1999), to allow for the remaining effects of turbulence and subanalysis scale features. A two-step analysis was made in which the observations were used twice, with the first analysis becoming the background for the second, for which the length scale and background error were halved. The analyses are only mildly sensitive to varying the assumed background and observation error statistics, which were chosen to give an analysis that fitted the observations reasonably well, and to achieve internally consistent statistics for the observation-background

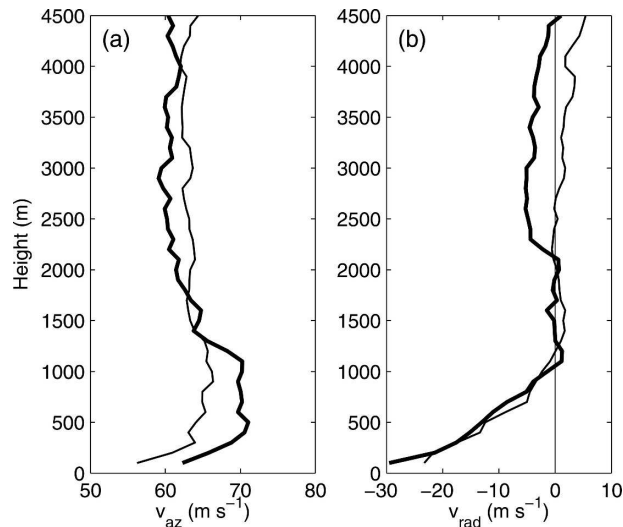


FIG. 10. Mean storm-relative (a) azimuthal and (b) radial wind, for the radii between 15 and 25 km (heavy line) and between 25 and 40 km (light line).

and observation–analysis differences. The differences between the observations and the analyses were carefully examined, and no spatial or temporal biases or trends were apparent.

Analyses of the storm-relative wind components are shown for representative levels in Fig. 13. The lowest level shown is 100 m, since the tendency for the eyewall sondes to fail near the surface results in insufficient data at lower levels for a satisfactory analysis. From 100-m to 1-km height, the radial component shows three distinct inflow maxima, approximately evenly distributed about the eyewall. These features are most marked from about 400- to 800-m height, but are easily seen at all levels except very near the surface. It is not clear whether the apparent weakness near the surface is real, or due to the reduced amount of data there. Analyses of equivalent potential temperature (θ_e , not shown) also show a wavenumber-3 feature, consistent with advection of θ_e by the radial flow asymmetry. The corresponding storm-relative azimuthal wind analyses show a similar feature. The analyses for the 500-m level, with the symmetric component removed, are shown in Fig. 14. It is apparent that the v asymmetry is of about half the amplitude and in approximate quadrature with the u asymmetry. Figure 14 also shows the divergence, vorticity, and asymmetric vorticity at 500 m. The total vorticity is dominated by the marked maximum at the center, but the asymmetric vorticity and divergence

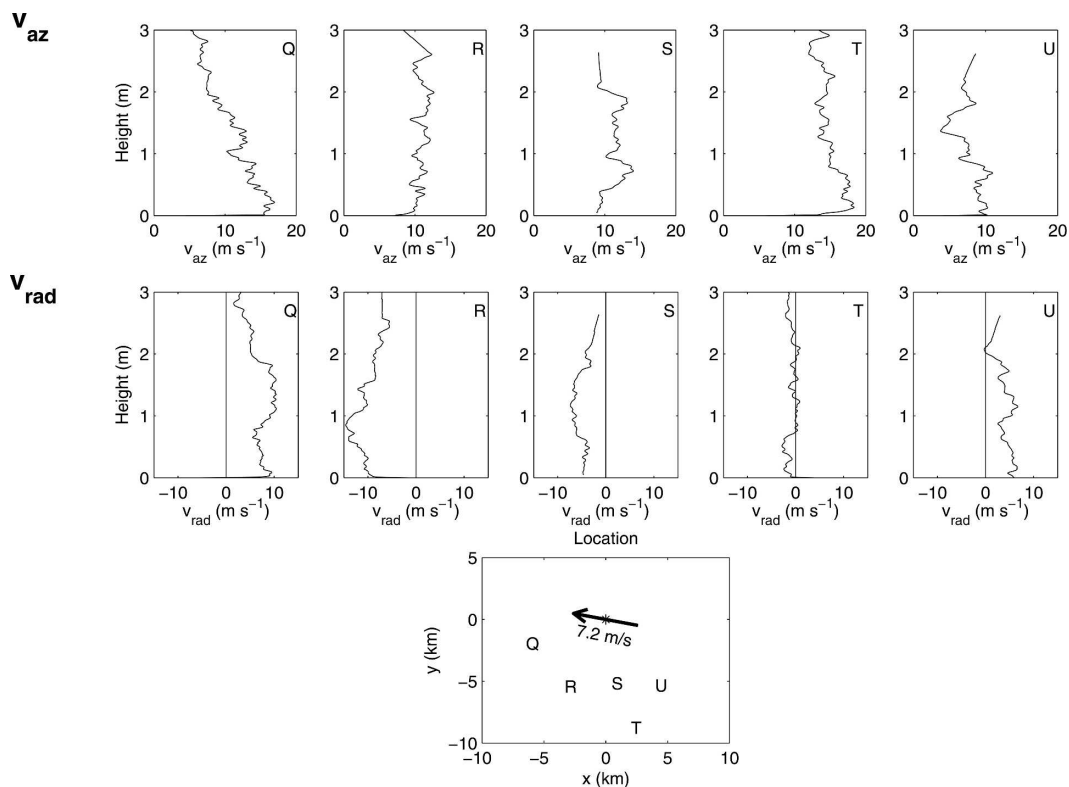


FIG. 11. Dropsonde observations of storm-relative (top) azimuthal and (middle) radial components, for observations in the eye. (bottom) The storm-relative dropsonde positions as the instrument passed through 1-km height, and the storm motion.

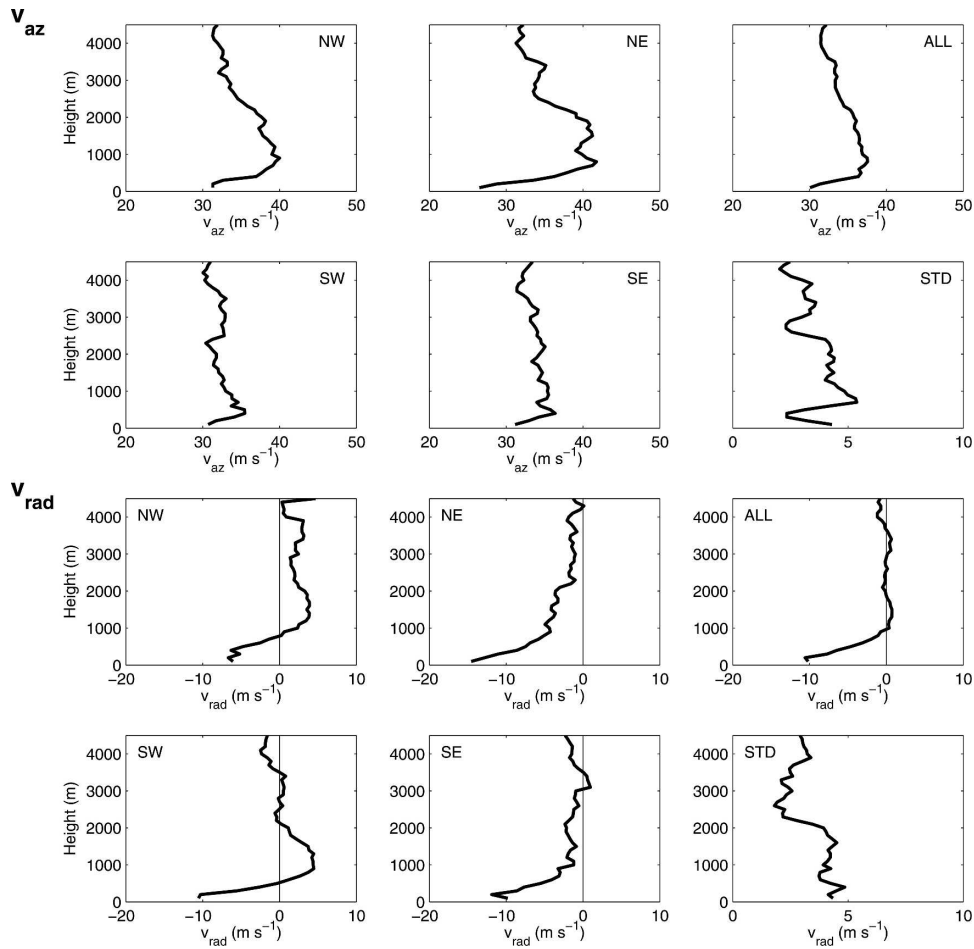


FIG. 12. The same as Fig. 9, except for observations between 40- and 100-km radius.

show a clear wavenumber-3 asymmetry near the RMW. In addition, the divergence plot shows a broad area of divergence ahead of the storm, consistent with the relatively weak low-level inflow in the western quadrants apparent in Fig. 12.

At and above 1 km, the relative radial flow consists mainly of throughflow from the right-rear to left-forward quadrant, although a trace of the wavenumber-3 pattern is still visible below 1.5 km (Fig. 13). This throughflow rotates anticyclonically with height at a rate of about 40° km⁻¹ to 4-km height (the highest analyzed). At these levels, the azimuthal flow also has a wavenumber-1 asymmetry, which strengthens and rotates anticyclonically with height, in near-quadrature with the radial flow asymmetry.

Interpretation of the wavenumber-3 asymmetry below 1 km is difficult. It is of amplitude about 8 m s⁻¹ in the u component, and half that in v . Linearization of the equations of motion [e.g., K01, his Eqs. (5) and (6)] suggests that the ratio of the u and v asymmetries is $[(f + 2V/r)/(f + V/r + \partial V/\partial r)]^{1/2}$, which is approximately

1 inside the eye and increases rapidly across the RMW to about 2, consistent with the analyses. The data were taken over a period of approximately 6 h, and each of the inflow maxima is defined by several observations, so for them to be a rotating or transient feature, they would need to have been remarkably well coordinated with the sampling pattern. Careful examination of the data suggests that it is unlikely that they are rotating around the storm, but it is impossible to completely rule this out. The inflow maxima have good vertical consistency and the analyses were prepared independently at each level, so they are unlikely to be an analysis artifact. Speculation as to their cause is difficult. If they were rotating features that the sampling strategy has aliased to an apparently stationary state, then vortex Rossby waves or weak eyewall mesovortices would be a possibility, except that they are confined to below 1 km. Environmental shear can cause asymmetries, but neither the wavenumber-3 nor the shallow vertical extent are consistent with this cause. The location within the BL suggests asymmetric surface friction as a candidate,

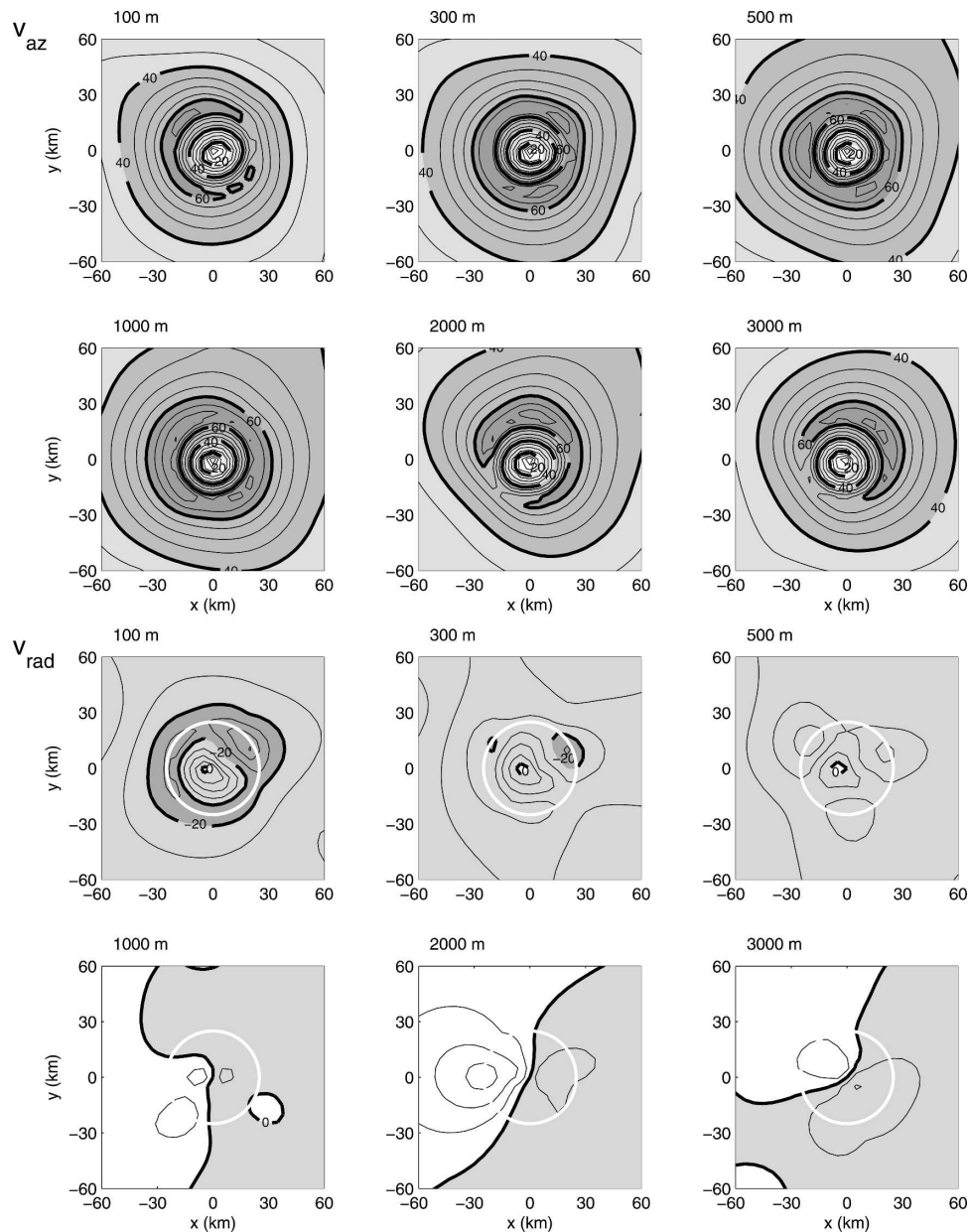


FIG. 13. Analyses of the storm-relative (top two rows) azimuthal and (bottom two rows) radial wind component at representative levels as shown. The contour interval is 5 m s^{-1} with heavy labeled contours at multiples of 20 m s^{-1} . Darker shading corresponds to (upper) stronger winds and (lower) stronger inflow. The white circle in the lower panels indicates the approximate RMW.

but this forcing is at wavenumber 1, so a nonlinear interaction would be necessary to generate the wavenumber 3. Shapiro (1983) showed using a two-dimensional depth-averaged model of the TCBL that nonlinear interactions became important for more rapidly moving storms, although he considered only the first two azimuthal wavenumbers. At over 7 m s^{-1} , Hurricane Georges was relatively rapidly moving, so

the hypothesis of a nonlinear interaction within the BL seems plausible.

The anticyclonically rotating with height, wavenumber-1, asymmetry above 1 km is similarly either stationary, or apparently so due to the aliasing of a propagating feature by the sampling. A similar feature occurred in Hurricane Mitch, and discussion of the possible cause will be deferred until Part II.

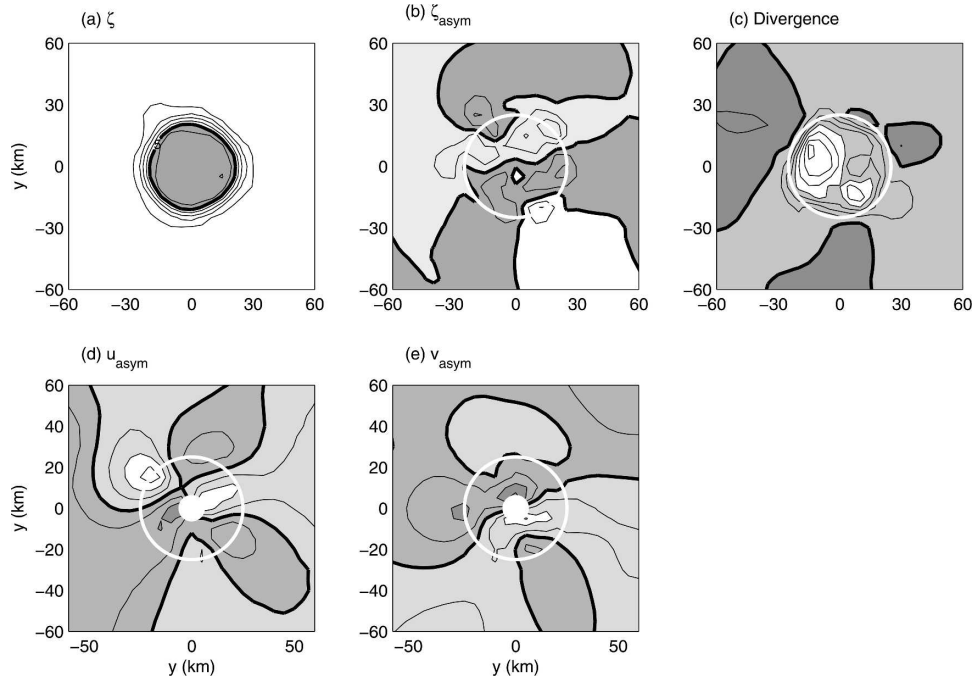


FIG. 14. Wind structure at 500 m: (a) relative vorticity, (b) asymmetric relative vorticity, (c) horizontal divergence, (d) asymmetric radial wind component, (e) asymmetric azimuthal wind component. Contour intervals are (a) 10^{-3} s^{-1} , (b) $2.5 \times 10^{-4} \text{ s}^{-1}$, (c) $2.5 \times 10^{-4} \text{ s}^{-1}$, (d) 2 m s^{-1} , (e) 2 m s^{-1} . The zero contour and in (a), the $4 \times 10^{-3} \text{ s}^{-1}$ contour, are shown heavy. The white circle shows the approximate RMW, and the central white dot in (d), (e) obscures the singularity at the origin in cylindrical winds. Darker shading corresponds to higher numerical values. The storm motion is toward the WNW at about 7 m s^{-1} .

e. Wind reduction factor

The ratios of the earth-relative wind speed at 100 m, to that at 1500 and 3000 m, were calculated from the above wind analyses and are shown in Fig. 15. The wind speed at 100 m is expected to be similar in distribution but somewhat stronger than that at the surface, since Powell et al. (2003) have shown that the mean wind profile in TCs is close to logarithmic in height up to 100 m. However, there is a considerable level of uncertainty in the drag coefficient at these wind speeds and hence in the slope of the logarithmic wind profile, so it was deemed unwise to assume a profile and adjust the 100-m wind to 10 m.² These wind speed ratios will be called wind reduction factors (WRF), to distinguish them from a surface (actually 10 m) wind factor. The reference heights of 1500 and 3000 m were chosen as typical of reconnaissance flight levels.

These analyses of WRF are in good agreement with the SWF predictions of K01 and KW01, with the ex-

pected increase toward the storm center and the left-right asymmetry both clearly apparent. The maximum appears to lie toward the left rear, rather than the left front, because the comparison here is between measured winds at two heights, rather than the gradient wind and a near-surface wind; thus comparison with Fig. 12b of KW01 is most appropriate. That figure shows a band of low values of the SWF extending from the minimum to the right around to the left front of the storm, and a maximum extending from the left-front eyewall outward to the left rear. The similarity to Fig. 15a here is striking. The secondary maximum in the left rear quadrant at a radius of approximately 90 km is defined by three observations, profiles B, C, and E, taken over five hours. Thus it is not a transient feature, but rather is associated with the outer convective ring apparent on radar imagery and strongest to the rear of the storm.

4. Analysis of balance

a. Analysis technique

The data are relatively few and are unevenly distributed in space, so it was decided to fit the Willoughby et

² The missing lower parts of the observed profiles were not filled in with a logarithmic profile for the same reason.

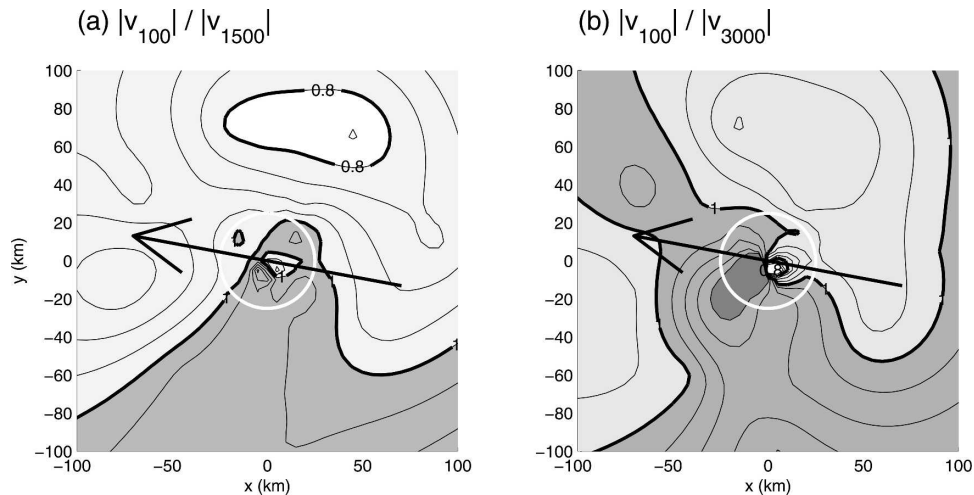


FIG. 15. Wind reduction factors. (a) The ratio of the 100-m earth-relative wind speed to that at 1.5 km. (b) The ratio of the 100-m earth-relative wind speed to that at 3 km. Contour interval is 0.05, with multiples of 0.2 heavy and labeled. The white circle shows the approximate RMW and the arrow, the storm motion. Darker shading corresponds to higher values. Note the large area, particularly to the left of the track, where the 100-m wind speed exceeds that above the BL.

al. (2006) parametric profile (henceforth WDR profile) to the data, rather than analyzing to some grid. The WDR profile was designed specifically to accurately fit wind observations, and has been extensively tested on aircraft data. Here, it is used both in its original form as a wind profile, and in the equivalent pressure form found by radially integrating the gradient-wind equation. The profile (in either form) is fit to the observations using the Levenberg–Marquadt method (Press et al. 1992, section 15.5), and the derivatives with respect to the control variable were found as described by Kepert (2002, appendix 4.A2). The equation minimized for the pressure fits was

$$J(\mathbf{a}) = \sum_{i=1}^{n_{\text{obs}}} \frac{[p_i - p_w(r_i; \mathbf{a})]^2}{\sigma_p^2 + (\sigma_r \partial p_w / \partial r)^2}, \quad (2)$$

where p_i is the i th pressure observation at radius r_i , p_w is the pressure form of the WDR profile, \mathbf{a} is the vector of parameters for p_w , $\sigma_p = 1$ hPa is the estimated standard deviation of the pressure observation error, $\sigma_r = 2$ km is the estimated standard deviation of the position error (including track uncertainties), and n_{obs} is the number of observations. The choice of $\sigma_p = 1$ hPa is larger than Hock and Franklin (1999) suggest, but the residual differences between the upward and downward integrations, the need to include errors of representation, and the uncertainty in the splash pressure due to the wavy sea surface support this choice. A similar equation was used for the wind fits, in which the

pressure observations are replaced by the storm-relative azimuthal component of the wind observations, the pressure form of the WDR profile is replaced by the wind form, and an observation error standard deviation of $\sigma_v = 5$ m s⁻¹ is used. This value is also higher than Hock and Franklin (1999) give for the dropsonde accuracy because of the necessity to allow for errors of representation due to turbulence, and is consistent with Fig. 9. Note that (2) includes the effects of observational error in both pressure and location. While the errors in the dropsonde location are negligible for this purpose, the track is not as accurately known; the results of Kepert (2005) suggest that $\sigma_r = 2$ km is appropriate. Including this component of error leads to a slightly greater gradient in the fitted pressure profile near the RMW than if it is omitted (Kepert 2002, appendix 4.A3).

The WDR wind profile may be written

$$\begin{aligned} v_1(r) &= (v_{m1} + v_{m2})(r/r_m)^{n_1} \\ v_2(r) &= v_{m1} \exp[(r_m - r)/L_1] + v_{m2} \exp[(r_m - r)/L_2] \\ v(r) &= [1 - w(r)]v_1(r) + w(r)v_2(r). \end{aligned} \quad (3)$$

The profile consists of the weighted mean of an eye profile v_1 with shape defined by n_1 ($1 < n_1 < 2$), and an outer wind profile v_2 , which is the sum of two exponentials of length scales L_1 and L_2 , and amplitudes v_{m1} and v_{m2} . The maximum wind is $v_m = v_{m1} + v_{m2}$ at the RMW r_m . The weighting function w is a nonic polynomial,

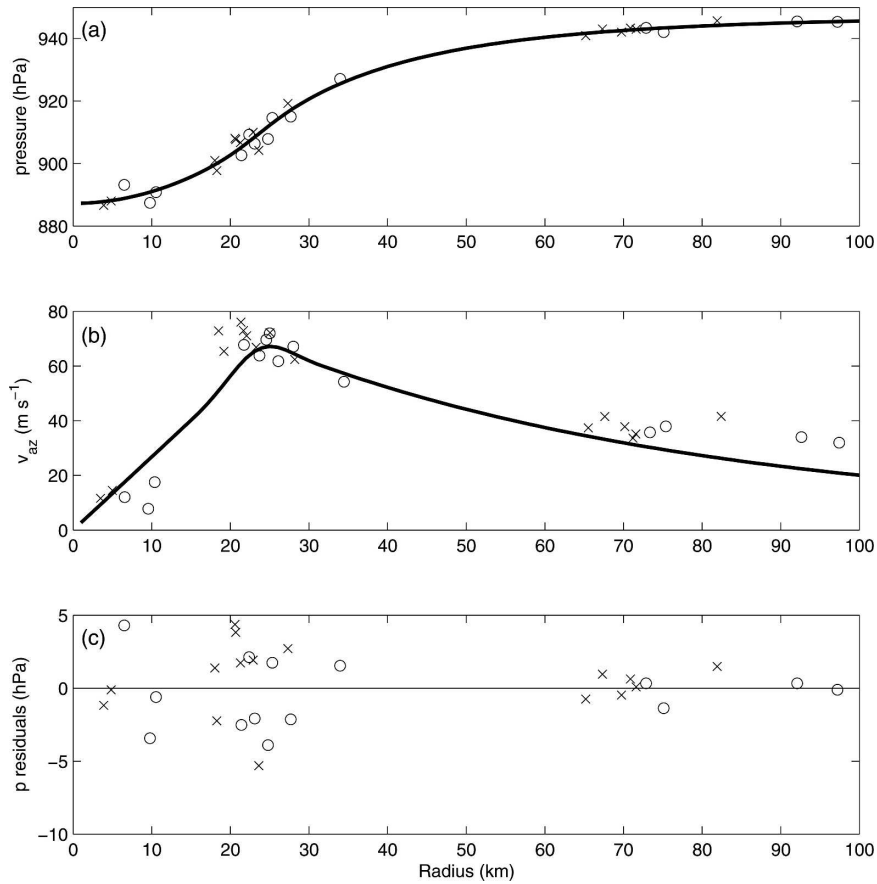


FIG. 16. (a) Observations of pressure from the early (○) and late (×) periods, at a height of 500 m in Hurricane Georges, together with the best-fit WDR radial pressure profile. (b) Observations of storm-relative azimuthal wind from the early (○) and late (×) periods, together with the gradient-wind speed calculated from the fitted pressure curve. (c) Differences between the observed and fitted pressures.

which increases monotonically from 0 to 1 across a blending zone of width $2L_b$ that contains r_m , with four continuous derivatives at each end of the blending zone. The location of the blending zone is determined by the requirement that the maximum wind occur at r_m , and found by solving $\partial v/\partial r = 0$ at r_m . The components of the control vector in (2) are thus $\mathbf{a} = (v_{m1}, L_1, v_{m2}, L_2, r_m, n_1, p_c, T_v, L_b)$. Physically, the eye profile v_1 can range from solid-body rotation ($n_1 = 1$) to something more bowl shaped. The profile with only one exponential (i.e., $v_{m2} = 0$) is often adequate except for storms with a large radius of gales. H. E. Willoughby (2002, personal communication) suggests L_2 would normally be several hundred kilometers, and recommends 5 km for the blending zone half-width, L_b . An equivalent radial pressure profile was obtained by radially integrating the gradient wind equation applied to (3). For this integration, the virtual temperature T_v is assumed to be constant and the equation of state used to find the

density, while the central pressure p_c provides the integration constant (Kepert 2002, appendix 4.A2).

b. Gradient-wind equation I: Pressure analysis

Radial pressure profiles were fit to the pressure data at multiple levels, and the gradient-wind speed calculated and compared to the storm-relative azimuthal wind observations. Initially, observations from both periods were analyzed together, but this produced incorrect results due to small changes in the cyclone structure between the periods (Fig. 16). The pressure profile clearly fits the observations well, and analysis of the residuals shows that both the 15–40-km and 60–100-km bands are uncorrelated with radius, so the gradients in these bands are accurately estimated. The lack of correlation in the residuals, considered as a whole, can be seen in Fig. 16c. However, it is clear that the pressure near the RMW rose between the early and late periods as the RMW contracted, and that the residuals from

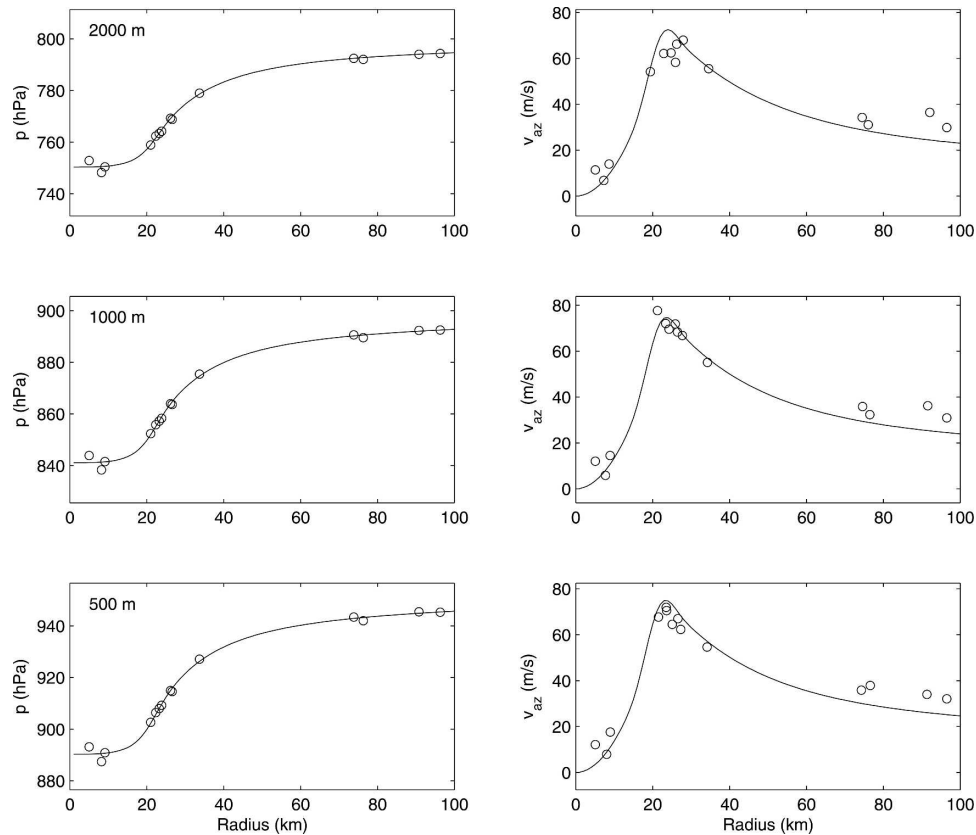


FIG. 17. (left) Observations of pressure at (top) 2 km, (middle) 1 km, and (bottom) 500 m, together with fitted curves, for the early period. (right) Observations of storm-relative azimuthal wind, together with the gradient-wind speed, at the same heights.

each period (considered separately) are correlated with radius, so the fitted curve underestimates the radial pressure gradient in both periods, and the apparent supergradient flow near the RMW is spurious. Thus it is necessary to consider the periods separately.

The pressure profile was then fit to just the observations from the first observing period, at every 100 m from the surface to 3 km. It was impractical to fit all the parameters, as the Hessian matrix in the iteration became singular, so $L_2 = 400$ km and $L_b = 9$ km, found from fitting the flight-level data, were prescribed. The reasonable constraints that $L_1 > 15$ km and $1 < n_1 < 2$ were applied.

The observations of pressure and wind at 500 m, 1 km, and 2 km, together with the fitted pressure profiles and their corresponding gradient-wind profiles, are shown in Fig. 17. At all levels, the storm-relative azimuthal wind observations in the vicinity of the RMW are at or slightly less than the estimated gradient-wind speed. This unexpected result is discussed below. The apparent supergradient flow in the outer core may be spurious, since with only four observations, widely

spaced in azimuth, any small asymmetries in the storm would result in an inaccurate estimate of the azimuthal-mean pressure gradient there.³ The vertical profiles of the fitted maximum gradient wind and its radius, together with the fitted value of the cost function show good vertical consistency, and that the maximum gradient wind slowly decreases with height while its radius increases, as would be expected (Fig. 18). The general decrease with height of the cost function implies that the observations fit the profile better further away from the surface. Lorenc (1986) discusses two sources of observational error relevant to objective analysis: instrumental and representational. The latter arises from phenomena on scales that are unresolved by the analysis. All except one of the pressure–height profiles used were integrated upward from the surface, eliminating

³ It is possible that the outer rainbands are in the process of organizing into an outer wind maximum, which could be supergradient in the upper boundary layer through the mechanism studied by K01 and KW01. Unfortunately there is insufficient data to examine this.

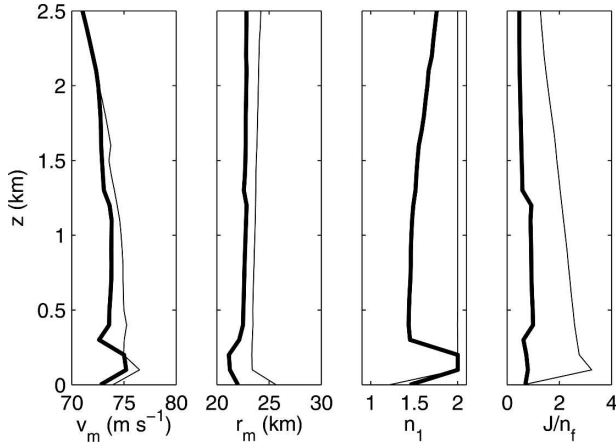


FIG. 18. Selected fitted parameters in the WDR parametric profile, for fits of the pressure form of the WDR parametric profile to the early (thin line) and late (thick line) dropsonde pressure data. From left, the maximum wind, the radius of maximum winds, the eye shape parameter and the goodness-of-fit J divided by the number of degrees of freedom.

the possibility that instrument error (here including the hydrostatic integration) decreases with height. The decrease with height could be because the representational errors are larger near the surface, or because this component of the error is proportional to the pressure, as would occur if the unresolved features were approximately balanced and of roughly constant velocity amplitude with height.

The fitted parameters from the late period are also shown in Fig. 18, and again there is good vertical consistency and physically reasonable height variation. The flow near the RMW is now found to be indistinguishable from gradient balance above 400 m. Gradient and observed winds are compared for the same three levels in Fig. 19. The outer core winds are closer to gradient balance than in the earlier case, probably because the greater amount of data gives a more reliable estimate of the radial pressure gradient now. Note that J/n_f is close to constant with height in the late period, and smaller than in the early period, suggesting that the hypothesized unresolved low-level features of the early period are now weaker. This change is likely related to the decrease in the eye shape parameter n_1 , implying reduced barotropic instability of the inner edge of the RMW.

Several components of the analysis technique have the effect of increasing the fitted pressure gradient, and hence the gradient wind speed, near the RMW. In particular, radial mislocation of the data relative to the RMW, either by combining the two measurement periods, or by less careful determination of the track, produces more diffuse data near the RMW, a weaker fitted

$\partial p/\partial r$ there, and apparently more supergradient flow than found. The inclusion of the location error in (2) also leads to an increase in the estimated gradient wind (Keper 2002, appendix 4.A3) by about 1 m s^{-1} . Similar analyses were carried out using the Holland (1980) parametric profile, and the WDR profile with only a single exponential (i.e., v_{m2} forced to be 0). In the former case, a deep layer of markedly supergradient flow was diagnosed during both periods, while in the latter, a shallower layer of less strongly supergradient flow was found. However, close examination of the residuals from the fit in the vicinity of the RMW showed that a part of the radial pressure gradient there had not been fitted, since these profiles lacked sufficient flexibility to conform to both the strong gradient near the RMW and the observations in the outer core. Thus the analysis technique is conservative from the point of view of searching for supergradient winds, in that the omission or alteration of components of it results in the diagnosis of a weaker gradient wind, and apparently more supergradient flow, than was actually found.

c. Gradient-wind equation II: Wind analysis

Gradient balance is now analyzed the opposite way, by analyzing the wind field and radially integrating the gradient-wind equation to obtain the gradient pressure profile, which is compared to the dropsonde pressure–height data. The two observation periods are again analyzed separately. The vertical profiles of the fitted parameters for both periods shown in Fig. 20, and display reasonable vertical consistency, a tendency for the RMW to increase with height, and the maximum wind peaking at 400 m and 1.1 km (earlier period) and 500 m (later period), before decreasing with height. The decreased barotropic instability of the eye with time, found in the pressure fits, can also be seen here. The peak at 1.1-km altitude for the earlier period may be spurious, as it is significantly affected by the sharp maximum in profile H, which is probably unrepresentative of steady flow.

Radial integration of the gradient-wind equation requires a known pressure at some radius. Using an observed pressure within the eye was unsatisfactory because the fitted profile shape n_1 inside the RMW is relatively noisy, in turn because the observations that affect n_1 are all very near the center, and random variations in them produce changes in n_1 that lead to an uncertainty of a few hectopascals in the pressure rise from the center to the RMW. Thus the integration was performed inward from the mean radius and pressure of the outer core observations.

The wind observations and fitted profiles, and pressure observations and gradient pressure profile are

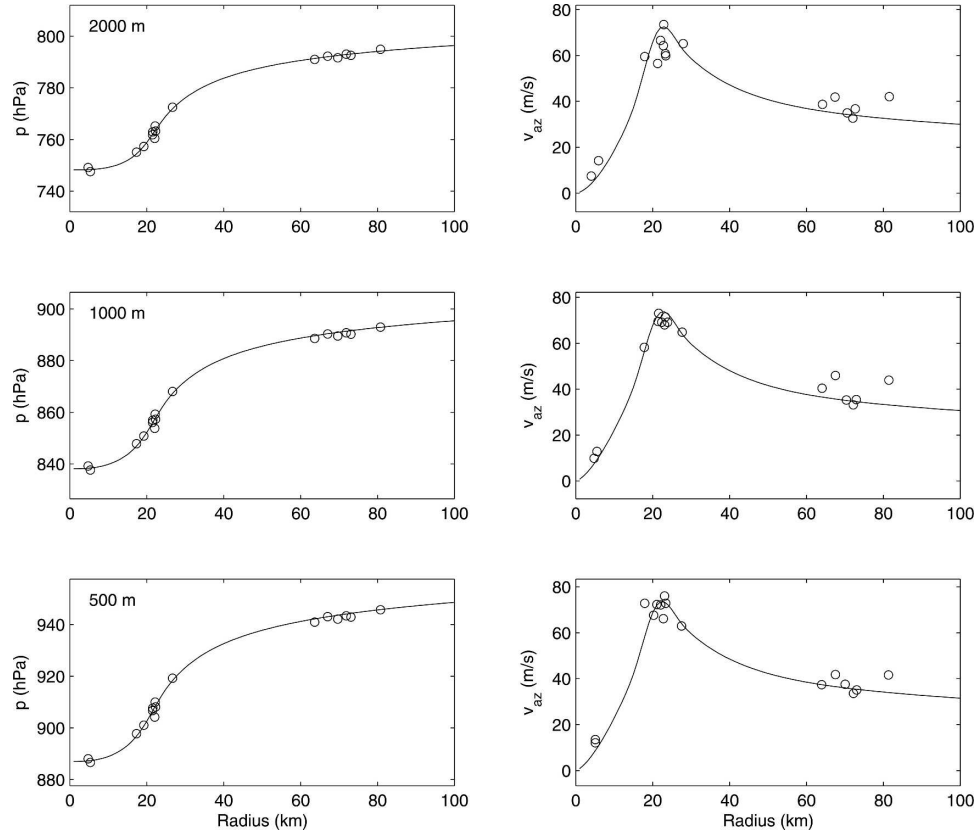


FIG. 19. Same as Fig. 17, but for the late period.

shown in Figs. 21 and 22 for the same levels as before. The pressures calculated by integrating the gradient-wind equation agree well with the observations, particularly in the earlier period. A systematic difference of about 3 hPa between the pressure observations near

the RMW and the calculated gradient pressure in the late period could be consistent with weakly supergradient flow, or due to the fitted winds being a little too strong in the data void centered around radius 50 km. This difference is thus not regarded as evidence of supergradient flow.

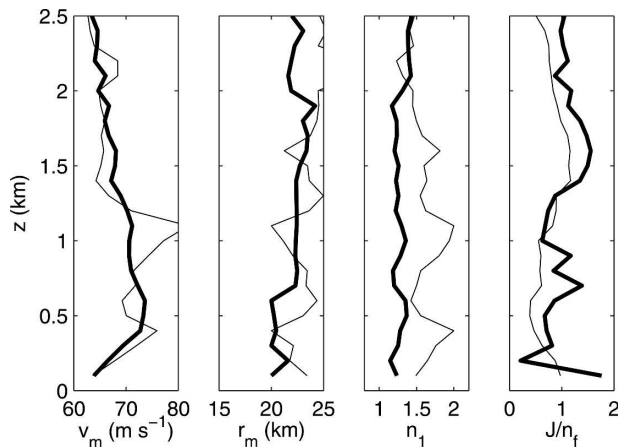


FIG. 20. Same as Fig. 18, but for the fits of the WDR wind profile to the dropsonde azimuthal wind component observations from the early (light) and late (heavy) periods.

5. Model simulations

The model of KW01 was modified to allow forcing by the WDR profile. There is a choice of parameters for the WDR profile, as this has been fitted every 100 m in height to pressure and wind data for both periods, and to aircraft data. The values $v_{m1} = 35 \text{ m s}^{-1}$, $L_1 = 24 \text{ km}$, $v_{m2} = 35 \text{ m s}^{-1}$, $L_2 = 800 \text{ km}$, $r_m = 23.2 \text{ km}$, and $n_1 = 0.9$ were chosen as a reasonable consensus. Here, L_1 was set a little larger than found in the fits to avoid inertial instability, and n_1 to be slightly less than 1 to avoid barotropic instability. The storm translation was from the track analysis.

The observed and modeled profiles of storm-relative azimuthal and radial wind components for the soundings near the RMW are compared in Figs. 7 and 8. To

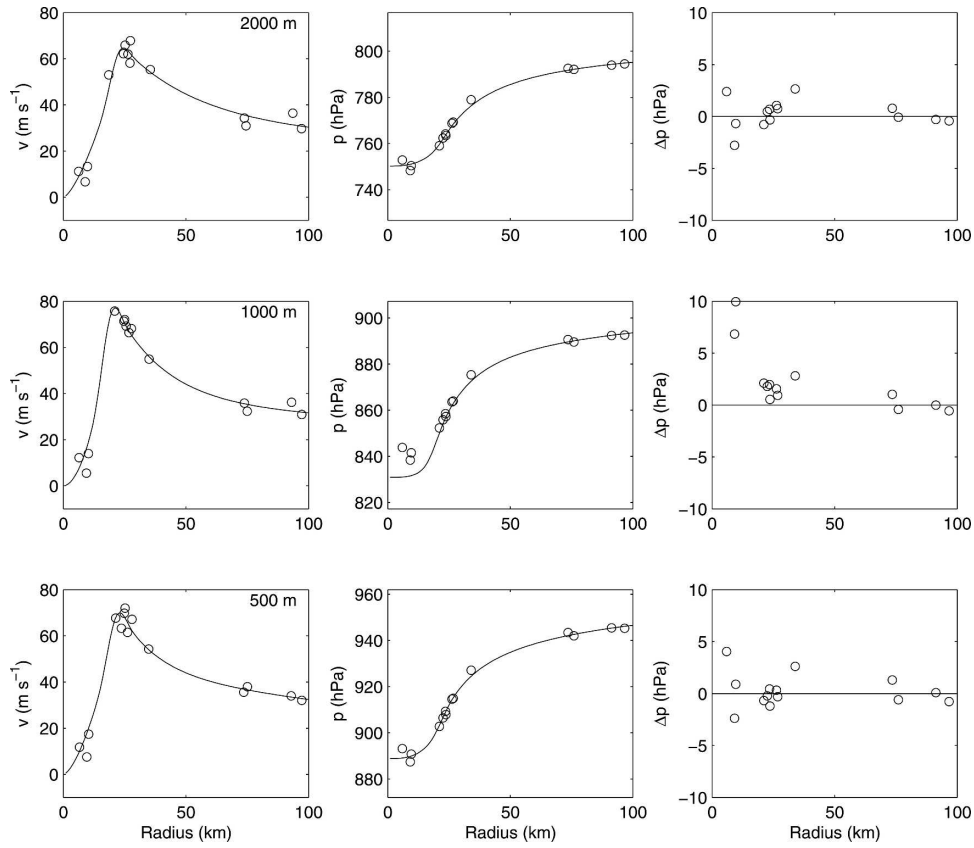


FIG. 21. Fits of the WDR wind profile at (top) 2 km, (middle) 1 km, and (bottom) 500 m, to observations from the early period. (left) Observed and fitted storm-relative azimuthal wind. (center) Pressure observations and gradient pressure curve. (right) Differences between the gradient pressure and the observations.

the north of the storm (profiles P, A, B, and C) the agreement in both wind components is very good. The weak azimuthal maximum near 500-m height has been faithfully captured, and the depth of the inflow layer is correct, albeit too strong in profiles B and C. Ahead of the storm (D to G) the inflow is well handled, but the outflow layers in the upper part of profiles E and G are missing, and the azimuthal flow is less well predicted. The model partially captures the pronounced low-level azimuthal maximum to the south of the storm (H to M). The difficulty in this region may be partly due to the very sharp gradients coupled with small errors in navigation. The successful depiction of the marked outflow in profile H is marred by an overprediction of outflow in profiles I, J, and K. To the rear, profiles N and O were not well handled, with neither the very strong inflow nor the marked decrease in azimuthal component above 500 m being captured. The radar imagery (Fig. 3) shows a convective maximum in this area, which would modify the winds in its vicinity, and is probably part of the reason for the poor performance

here. A further reason is the model's failure to produce the significant azimuthal wavenumber-3 asymmetry in the inflow below 1 km.

The modeled winds were also compared to the outer core observations, but this was less successful and is not shown. The main reason for the relatively poor comparisons is probably the convective band near a radius of 70 km in the eastern half of the storm (Fig. 3), which had strengthened and contracted slightly by the later period. While many of the outer core observations were taken in the vicinity of this band, it is not represented in the WDR profile used to force the model.

The analysis of balance in section 4 produced the result that the winds in the upper BL near the eyewall were not supergradient, apparently contrary to the analysis of K01 and KW01. The ratio of the simulated azimuthally averaged azimuthal wind component to the gradient wind is plotted in Fig. 23a, which shows that the model is here predicting a quite different distribution of supergradient flow to the cases considered by KW01. Near and immediately outside of the RMW, the

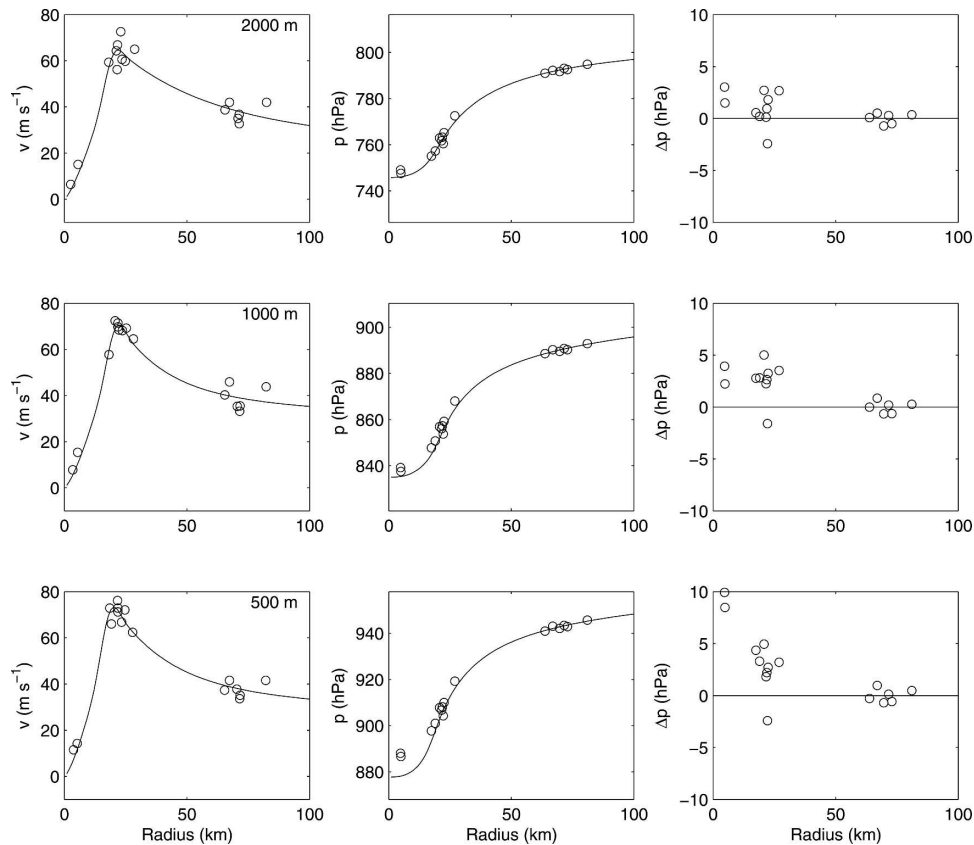


FIG. 22. Same as Fig. 20, but for the late period.

flow is predicted to be at most only a few percent supergradient, with a more strongly supergradient flow in the light winds near the center and a large area of moderately supergradient flow at radii greater than 80 km. KW01 diagnosed the cause of the supergradient flow as being advection of angular momentum in the frictionally driven inflow, and showed that a storm with a “peaked” wind profile produced markedly supergradient flow at the RMW but little outside, while a storm with a “flat” wind profile and hence a more widely distributed region of angular momentum gradient produced more widely distributed but less strongly supergradient flow. The radial profile of gradient wind used to force the model, together with the absolute angular momentum, is shown in Fig. 23b, and it is apparent that the outer part of Georges had a very slow decrease of wind speed with radius, and that there was a local minimum in the angular momentum gradient just outside the RMW. The lack of supergradient flow found is thus more consistent with the theory of KW01 than was at first apparent.

A similar simulation was undertaken with the model forced by a Holland (1980) profile fitted to the observations. While the predicted asymmetries were broadly

similar, the detailed agreement between model and observations was substantially worse (not shown). The BL wind structure is thus seen to be highly sensitive to small details of the storm structure.

6. Discussion

The dropsonde observations in Hurricane Georges have been compared with the predictions of K01 and KW01 in three ways. The first was a qualitative comparison of the shapes of the profiles, particularly the height and relative strength of the low-level jet, with the theory. It was shown by examining the individual profiles and mean profiles stratified by radius and/or azimuth that a substantial part of the large variability between individual profiles is due to the spatial structure of the storm, consistent with that predicted. In particular, the jet becomes closer to the surface toward the storm center and is significantly stronger (relative to the flow above the boundary layer) on the left of the storm than the right. Analyses of the observed wind reduction factor were similarly in good agreement with the results of K01 and KW01, showing both the predicted left–right asymmetry and the increase toward the center of the storm.

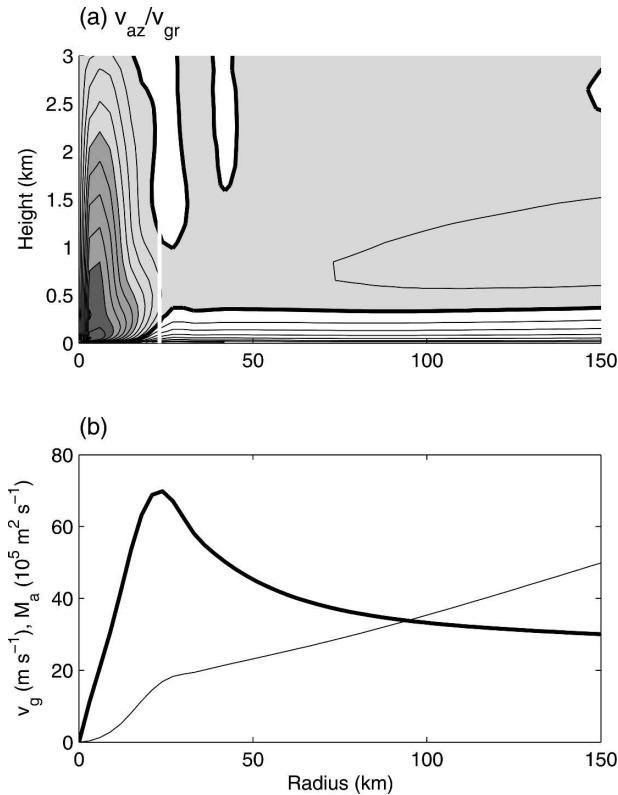


FIG. 23. (a) Radius–height section of the azimuthal-mean storm-relative azimuthal wind component, relative to the gradient wind, from the model simulation of the BL flow in Georges. Contour interval 0.05, contour of 1.0 is heavy, darker shading indicates higher values, RMW show as the vertical white line. (b) Storm-relative gradient wind speed (heavy, $m s^{-1}$) and absolute angular momentum (light, $10^5 m^2 s^{-1}$).

The main area of disagreement with the theory was the occurrence of an azimuthal wavenumber-3 asymmetry in the storm-relative flow, below about 1-km height near the eyewall. This feature was apparently stationary with respect to the storm, and about twice the amplitude in the radial, compared to the azimuthal, wind component. It was apparently not an eyewall mesovortex or vortex Rossby wave, nor caused by an environmental interaction, due to its shallowness. It may be the result of a nonlinear processes acting upon the basic motion-induced wavenumber-1 asymmetry.

Gradient balance was diagnosed by comparing the observed winds to an estimate of the gradient wind obtained from a pressure analysis, and by comparing the observed pressures to an estimate of the gradient pressure field obtained from a wind analysis. The results are consistent, in that the flow near the RMW above 400-m altitude seems to be very close to gradient balance in the later period, and slightly subgradient in the earlier. These results are apparently contrary to the

prediction of K01 and KW01 that the upper BL flow is supergradient.

The numerical model of KW01 was run with forcing provided by a pressure pattern and motion representative of Georges. The model did a good job of reproducing the main features of, and variation between, individual dropsonde profiles near the eyewall in both the azimuthal and the radial wind components. The model further predicted that the near-eyewall flow in Georges would be at most only a few percent supergradient, consistent with the observational analysis. This weak supergradient flow is in contrast to the cases considered by KW01, and is due to the particular angular momentum distribution in Georges, with a relatively slow decrease of wind speed outside the inner core and a minimum in the radial gradient of absolute angular momentum immediately outside of the RMW.

It is possible, but considered unlikely, that the apparent lack of supergradient flow is a consequence of the analysis technique. The hydrostatic integration necessarily ignores the effects of liquid water loading, and assumes hydrostatic balance. Although the method used for this integration yields improved consistency between the upward and downward integrations, differences of up to a few hectopascals remain and could be affecting the results. The amount of data is quite small, and is unevenly distributed in radius, so it is not possible to completely eliminate the possibility that overfitting is occurring; that is, that errors (instrumental or of representation) in the data result in a spurious increased pressure gradient in the fitted profile. For instance, if the vortex tilt is not taken account of, a weaker gradient is fitted and supergradient flow is diagnosed from about 500 to 1500 m, but a marked azimuthal wavenumber-1 pattern appears in the pressure residuals. Similarly, combining the two periods smears out the pressure gradient near the RMW, and produces some apparently supergradient flow. Neglecting the effect of position error in the fits leads to a weaker analyzed pressure gradient, as does using a different parametric profile. However, the time change and the vortex tilt are physically plausible features of the cyclone, the track uncertainty is real, and the WDR profile is the most realistic of those available. These elements of the analysis technique were carefully chosen to ensure that the findings were in no way biased toward the predictions of KW01 regarding supergradient flow; in this sense the analysis is highly conservative.

A companion paper (Part II) will present a similar analysis of Hurricane Mitch with contrasting results, notably in the distribution and extent of supergradient flow. Reasons for the differences between these storms are also discussed there.

Acknowledgments. This work formed part of my Ph.D. thesis at Monash University, and I am grateful to my supervisors, Greg Holland and Dale Hess, for their encouragement and helpful suggestions, and to my employer for allowing me paid leave for a part of it. The analysis would have been impossible without access to the high quality data obtained by the Hurricane Research Division (HRD) and Aircraft Operations Center (AOC) of the National Oceanographic and Atmospheric Administration (NOAA). I am full of admiration for the hard work and dedication of the flight and scientific crews in obtaining these data, and gratefully acknowledge the generosity of the HRD in making it so freely available. I thank James Franklin and Mike Black for advice on many aspects of the GPS dropsonde, Hugh Willoughby and Ed Rahn for providing advice on the parametric wind profile, and John Kaplan for advice on environmental wind shear. The environmental wind-shear was calculated from ERA-40 reanalysis data, kindly provided by the European Centre for Medium-Range Weather Forecasts.

REFERENCES

- Aberson, S., cited 1998: Mission summary Hurricane Georges 980919h. [Available online at http://www.aoml.noaa.gov/hrd/HFP98/980919h_sum.pdf.]
- Anthes, R. A., 1971: Iterative solutions to the steady-state axisymmetric boundary-layer equations under an intense pressure gradient. *Mon. Wea. Rev.*, **99**, 261–268.
- Black, M. L., cited 1998: Mission summary 981027I1 Hurricane Mitch modified eyewall vertical motion experiment. [Available online at http://www.aoml.noaa.gov/hrd/HFP98/981027i1_sum.pdf.]
- Bluestein, H. B., and F. D. Marks Jr., 1987: On the structure of the eyewall of Hurricane Diana (1984): Comparison of radar and visual characteristics. *Mon. Wea. Rev.*, **115**, 2542–2552.
- Daley, R., 1985: The analysis of synoptic scale divergence by a statistical interpolation procedure. *Mon. Wea. Rev.*, **113**, 1066–1079.
- , 1991: *Atmospheric Data Analysis*. Cambridge University Press, 457 pp.
- DeMaria, M., and J. Kaplan, 1999: An updated statistical hurricane intensity prediction scheme (SHIPS) for the Atlantic and eastern North Pacific basins. *Wea. Forecasting*, **14**, 326–337.
- Eliassen, A., and M. Lystad, 1977: The Ekman layer of a circular vortex: A numerical and theoretical study. *Geophys. Norv.*, **31**, 1–16.
- Emanuel, K. A., 1986: An air–sea interaction theory for tropical cyclones. Part I: Steady-state maintenance. *J. Atmos. Sci.*, **43**, 585–604.
- Frank, W. M., and E. A. Ritchie, 2001: Effects of vertical wind shear on the intensity and structure of numerically simulated hurricanes. *Mon. Wea. Rev.*, **129**, 2249–2269.
- Franklin, J. L., M. L. Black, and K. Valde, 2003: GPS dropwindsonde wind profiles in hurricanes and their operational implications. *Wea. Forecasting*, **18**, 32–44.
- Gray, W. M., 1967: The mutual variation of wind, shear and baroclinicity in the cumulus convective atmosphere of the hurricane. *Mon. Wea. Rev.*, **95**, 55–73.
- , 1991: Comments on “Gradient balance in tropical cyclones.” *J. Atmos. Sci.*, **48**, 1201–1208.
- , and D. J. Shea, 1973: The hurricanes inner core region. II: Thermal stability and dynamic characteristics. *J. Atmos. Sci.*, **30**, 1565–1576.
- Hock, T. F., and J. L. Franklin, 1999: The NCAR GPS dropwindsonde. *Bull. Amer. Meteor. Soc.*, **80**, 407–420.
- Holland, G. J., 1980: An analytic model of the wind and pressure profiles in hurricanes. *Mon. Wea. Rev.*, **108**, 1212–1218.
- Jelesnianski, C., 1993: The habitation layer. *WMO Global Guide to Tropical Cyclone Forecasting*, G. J. Holland, Ed., WMO Tech. Doc. TCP-31, 356 pp.
- Jorgensen, D. P., 1984: Mesoscale and convective-scale characteristics of mature hurricane. Part I: General observations by research aircraft. *J. Atmos. Sci.*, **41**, 1268–1285.
- Keper, J. D., 2001: The dynamics of boundary layer jets within the tropical cyclone core. Part I: Linear theory. *J. Atmos. Sci.*, **58**, 2469–2484.
- , 2002: The wind-field structure of the tropical cyclone boundary-layer. Ph.D. thesis, Monash University, 350 pp.
- , 2005: Objective analysis of tropical cyclone location and motion from high density observations. *Mon. Wea. Rev.*, **133**, 2406–2421.
- , 2006: Observed boundary layer wind structure and balance in the hurricane core. Part II: Hurricane Mitch. *J. Atmos. Sci.*, **63**, 2194–2211.
- , and Y. Wang, 2001: The dynamics of boundary layer jets within the tropical cyclone core. Part II: Nonlinear enhancement. *J. Atmos. Sci.*, **58**, 2485–2501.
- Knaff, J. A., J. P. Kossin, and M. DeMaria, 2003: Annular hurricanes. *Wea. Forecasting*, **18**, 204–223.
- Kuo, H. L., 1971: Axisymmetric flow in the boundary layer of a maintained vortex. *J. Atmos. Sci.*, **28**, 20–41.
- , 1982: Vortex boundary layer under quadratic surface stress. *Bound.-Layer Meteor.*, **22**, 151–169.
- Landsea, C. W., J. L. Franklin, C. J. McAdie, J. L. Benen II, J. M. Gross, B. R. Jarvinen, J. P. Dunion, and P. P. P. Dodge, 2004: A reanalysis of Hurricane Andrew’s (1992) intensity. *Bull. Amer. Meteor. Soc.*, **85**, 1699–1712.
- Lorenc, A. C., 1981: A global three-dimensional multivariate statistical interpolation scheme. *Mon. Wea. Rev.*, **109**, 701–721.
- , 1986: Analysis methods for numerical weather prediction. *Quart. J. Roy. Meteor. Soc.*, **112**, 1177–1194.
- Marks, F. D., R. A. Houze, and J. F. Gamache, 1992: Dual-aircraft investigation of the inner core of Hurricane Norbert. Part I: Kinematic structure. *J. Atmos. Sci.*, **49**, 919–942.
- Mitsuta, Y., T. Suenobu, and T. Fujii, 1988: Supergradient surface wind in the eye of a typhoon. *J. Meteor. Soc. Japan*, **66**, 505–508.
- Montgomery, M. T., H. D. Snell, and Z. Yang, 2001: Axisymmetric spindown dynamics of hurricane-like vortices. *J. Atmos. Sci.*, **58**, 421–435.
- Pasch, R. J., L. A. Avila, and J. L. Guiney, 2001: Atlantic hurricane season of 1998. *Mon. Wea. Rev.*, **129**, 3085–3123.
- Powell, M. D., 1980: Evaluations of diagnostic marine boundary layer models applied to hurricanes. *Mon. Wea. Rev.*, **108**, 757–766.
- , S. H. Houston, and T. A. Reinhold, 1996: Hurricane Andrew’s landfall in south Florida. Part I: Standardizing measurements for documentation of surface wind fields. *Wea. Forecasting*, **11**, 304–328.

- , P. J. Vickery, and T. A. Reinhold, 2003: Reduced drag coefficient for high wind speeds in tropical cyclones. *Nature*, **422**, 279–283.
- Press, W. H., S. A. Teukolsky, W. Y. Vetterling, and B. P. Flannery, 1992: *Numerical Recipes in C*. Cambridge University Press, 994 pp.
- Reasor, P. D., M. T. Montgomery, and L. D. Grasso, 2004: A new look at the problem of tropical cyclones in vertical shear flow: Vortex resiliency. *J. Atmos. Sci.*, **61**, 3–22.
- Rosenthal, S. L., 1962: *A Theoretical Analysis of the Field of Motion in the Hurricane Boundary Layer*. National Hurricane Research Project Rep. 56, Washington, DC, 12 pp.
- Shapiro, L. J., 1983: The asymmetric boundary layer under a translating hurricane. *J. Atmos. Sci.*, **40**, 1984–1998.
- Simmons, A. J., and J. K. Gibson, 2000: The ERA-40 project plan. ERA-40 Project Rep. Series 1, European Centre for Medium-Range Weather Forecasting, 63 pp.
- Wang, J., H. L. Cole, D. J. Carlson, E. R. Miller, K. Beierle, A. Paukkunen, and T. K. Laine, 2002: Corrections of humidity measurement errors from the Vaisala RS80 Radiosonde—Application to TOGA COARE data. *J. Atmos. Oceanic Technol.*, **19**, 981–1002.
- Willoughby, H. E., 1990: Gradient balance in tropical cyclones. *J. Atmos. Sci.*, **47**, 265–274.
- , 1991: Reply. *J. Atmos. Sci.*, **48**, 1209–1212.
- , 1995: Mature structure and evolution. *Global Perspectives on Tropical Cyclones*, R. L. Elsberry, Ed., WMO Rep. TCP-38, 21–62.
- , and M. Chelmow, 1982: Objective determination of hurricane tracks from aircraft observations. *Mon. Wea. Rev.*, **110**, 1298–1305.
- , R. W. R. Darling, and M. E. Rahn, 2006: Parametric representation of the primary hurricane vortex. Part II: A new family of sectionally continuous profiles. *Mon. Wea. Rev.*, **134**, 1102–1120.
- Zhang, D.-L., Y. Liu, and M. K. Yau, 2001: A multiscale numerical study of Hurricane Andrew (1992). Part IV: Unbalanced flows. *Mon. Wea. Rev.*, **129**, 92–107.